RESEARCH ARTICLE | OCTOBER 15 2024

Coarse-grained modeling of high-enthalpy air flows based on the updated vibrational state-to-state kinetics

Yifeng Huang ; Qizhen Hong ; Sangdi Gu ; Xiaoyong Wang ; Quanhua Sun

Physics of Fluids 36, 106133 (2024)
https://doi.org/10.1063/5.0230687

Physics of Fluids **ARTICLE** pubs.aip.org/aip/pof

Coarse-grained modeling of high-enthalpy air flows based on the updated vibrational state-to-state kinetics

Cite as: Phys. Fluids **36**, 106133 (2024); doi: 10.1063/5.0230687
Submitted: 25 July 2024 · Accepted: 27 September 2024 ·
Published Online: 15 October 2024

Yifeng Huang,[1] Qizhen Hong,[1,a)] Sangdi Gu,[2] Xiaoyong Wang,[1] and Quanhua Sun[1,3,a)]

AFFILIATIONS

[1] State Key Laboratory of High Temperature Gas Dynamics, Institute of Mechanics, Chinese Academy of Sciences, 100190 Beijing, China
[2] Department of Aeronautical and Aviation Engineering, The Hong Kong Polytechnic University, Kowloon, Hong Kong, China
[3] School of Engineering Science, University of Chinese Academy of Sciences, Beijing 100049, China

[a)] **Authors to whom correspondence should be addressed:** hongqizhen@imech.ac.cn and qsun@imech.ac.cn

ABSTRACT

The state-to-state (StS) model can accurately describe high-temperature thermochemical nonequilibrium flows. For the five-species air gas mixture, we develop a comprehensive database for the state-specific rate coefficients for temperatures 300–25 000 K in this paper. The database incorporates recent molecular dynamics simulations (based on the *ab initio* potential energy surfaces) in the literature, and theoretical methods, including the forced harmonic oscillator model and the Marrone–Treanor model, are employed to complement the rate coefficients that are unavailable from molecular dynamics calculations. The post-shock StS simulations using the present database agree with the experimental NO infrared radiation. Based on this updated StS kinetics database, we investigate the post-shock high-enthalpy air flows by employing both the StS and coarse-grained models (CGM). The CGM, which lumps molecular vibrational states into groups, shows results that align with the StS model, even utilizing only two groups for each molecule. However, the CGM-1G model, with only one group per molecule and belonging to the multi-temperature model (but uses StS kinetics), fails to reproduce the StS results. Analysis of vibrational energy source terms for different kinetic processes and fractions of vibrational groups reveals that the deficiency of the CGM-1G model stems from the overestimation of high-lying vibrational states, leading to higher dissociation rates and increased consumption of vibrational energy in dissociation. Furthermore, the presence of the Zeldovich-exchange processes indirectly facilitates energy transfer in N_2 and O_2, a phenomenon not observed in binary gas systems. These findings have important implications for developing the reduced-order model based on coarse-grained treatment.

I. INTRODUCTION

In hypersonic flows, many physicochemical processes occur behind the intense shock wave, such as internal energy transfers, chemical reactions, ionization, and radiative emission.[1] The characteristic timescales of these microscopic phenomena can deviate by orders of magnitude, which results in the gas system deviating from local thermal and chemical equilibria. The thermochemical nonequilibrium effects, particularly internal energy relaxation and nonequilibrium chemical reaction rate, profoundly affect the aerodynamic characteristics of the hypersonic vehicle.[2] Consequently, accurately modeling the physicochemical processes is imperative for simulating the hypersonic flows.

The multi-temperature models have been widely used to describe the thermochemical nonequilibrium flows, with the Park two-temperature (2 T) model[3,4] being particularly prominent. Specifically, the Park 2 T model assumes equilibrium between translational and rotational energy modes of molecules at temperature T_{tr} (referred to as T hereafter) and equilibrium between vibrational and electronic energy modes at temperature T_{ve} (referred to as T_v hereafter),[4] and the energy distribution follows a Maxwell–Boltzmann distribution within each energy mode. Park's assumption is based on the fact that rotational energy levels are much closer together than vibrational or electronic levels, allowing rotational modes to quickly exchange energy (the energy gap law) with translational modes through collisions. In contrast, vibrational and electronic modes, having much higher energy levels, tend to equilibrate on a similar timescale but through slower processes. Consequently, alongside solving conservation equations for mass, momentum, and total energy, the 2 T model requires solving an additional conservation equation for vibration(-electronic) energy,[4] in which the energy source terms include the contributions from vibrational(-electronic) energy relaxation and vibration–chemistry coupling. Vibrational energy relaxation is commonly modeled using the Landau–Teller (L–T) model.[5] The vibration–chemistry coupling results from the influence of chemical reactions on vibrational energy and the influence of vibrational distribution function on reaction rates (e.g., molecules with higher vibrational energy are more prone to dissociate[6]). Many vibration–chemistry coupling models have been developed so far, such as the Park model,[4] Marrone–Treanor (MT) model,[6] Macheret–Fridman model,[7] and their variants.[8,9] However, the accuracy of these (semi) empirical models typically relies on a few adjustable empirical parameters, which are subject to tuning (such as those appeared in obtaining the nonequilibrium factor), resulting in varying degrees of accuracy across different scenarios.[10]

Over the past two decades, the high-fidelity vibrational state-to-state (StS) model, incorporating a vibrational state-specific kinetic mechanism, has become prevalent.[11–14] By capturing the evolution of molecular internal energy states, this approach enables a more precise understanding of nonequilibrium evolution law and sidesteps the need for empirical assumptions used in the 2 T models. However, the accuracy of the StS calculations strongly depends on the precision of the rate coefficients for elementary reactions. The vibrational state-specific rate coefficients from *ab initio* calculations are becoming available for the inelastic, dissociation–recombination (DR), and chemical exchange processes, occurring in the non-ionized five-species air mixture (including N_2, O_2, NO, N, and O and all assumed to be in the electronic ground state) of interest in this study. For O_2–O and N_2–N collisions, Esposito *et al.*[15,16] calculated the complete sets of vibrational–translational (VT) energy exchange and dissociation rate coefficients using the quasi-classical trajectory (QCT) approach based on full-dimensional potential energy surfaces (PESs). For chemical exchange (Zeldovich-exchange, ZE) reactions, namely, O_2–N and N_2–O collisions, Bose and Candler[17,18] studied the dependence of rate coefficients on the vibrational state of N_2 and O_2 and the product vibrational energy distribution of NO using the QCT approach, which enables the derivation of vibrational state-specific rates. The aforementioned state-specific rate coefficients for O_2–O and N_2–N collisions and two ZE reactions have been adopted in the STELLAR database summarized by Da Silva *et al.*[19] In addition, Da Silva *et al.*[19] obtained the VT and dissociation rate coefficients for N_2–N_2, N_2–O_2, O_2–O_2, NO–N_2, and NO–O_2 collisions using the theoretical forced harmonic oscillator (FHO) model in their database. Note that, in the STELLAR database, the vibrational–vibrational–translational (VVT) energy exchange processes in the diatom–diatom collisions are reduced to VT processes, equivalent to that of diatom–atom collisions, and some StS processes (such as VT transition of O_2–N collision, etc.) are not considered. Recently, Gu *et al.*[20] utilized the FHO model to calculate VVT rate coefficients for N_2–N_2, N_2–O_2, and O_2–O_2 collisions and showed that the reduction of VVT transitions to VT transitions is a poor approximation for the test conditions. Molecular dynamic calculations for VVT rate coefficients for O_2–O_2[21] and N_2–N_2[22] collisions were performed by Hong *et al.* using the mixed quantum-classical (MQC) method (which capture quantum effects related to vibrational motion), but these data do not cover an extensive temperature range (limited to 100–7000 K). Moreover, since NO is a strong radiator behind the shock wave, accurate prediction of its formation is crucial for understanding the high-temperature radiation. However, the VVT processes for the NO-related collisions are seldom considered in the literature. For the ZE reactions of NO formation, the aforementioned Bose and Candler's QCT data[17,18] are out-of-data since the employed PESs are three decades old. Recently, Esposito and Armenise[23,24] revisited the O_2–N and N_2–O collisions using the QCT approach based on the newly developed PESs and obtained not only the ZE but also the VT and dissociation state-specific rate coefficients. These data for O_2–N and N_2–O collisions can readily replace and supplement the corresponding ones in the STELLAR database and will be adopted in this paper.

Based on the available data of state-specific vibrational–chemical kinetics (though usually some of the rate coefficients are not derived from the *ab initio* calculations but only using the semiempirical or empirical methods and some of the StS processes are not taken into account), the StS calculations have been applied for shock-heated air flows in the literature.[12–14,20,25–29] Kunova and Nagnibeda[25] studied the nonequilibrium flows of the five-species air mixture $N_2(v)/O_2(v)/NO(v)/N/O$ behind shock waves by taking into account the StS vibrational–chemical kinetics and found that the free-stream vibrational excitation dramatically changes the post-shock relaxation zone structure. Su *et al.*[14] conducted vibrational StS modeling of the shock-heated air flows, specifically emphasizing NO formation. Their study revealed that NO formation is sensitive to the adopted rate coefficients, particularly for ZE reactions, and the StS model predicts greater NO formation and faster relaxation than the multi-temperature model. Campoli *et al.*[26] examined various state-resolved models for vibrational–chemical kinetics for the post-shock five-component air mixture and validated them against experimentally measured NO radiation. However, the results failed to give a unique recommendation on choosing the best StS model under arbitrary free-stream conditions. Gu *et al.*[20] integrated VVT transitions into the StS model and investigated their effect on shock-heated air flows. Restricting the quantum jumps of VVT transitions to only 5 can still yield post-shock macroscopic quantities with an acceptable accuracy compared to the unrestricted results across all tested conditions.[20] Moreover, Torres *et al.*[30] performed direct molecular simulations based on the available *ab initio* PESs for chemically reacting five-species air flows and extracted macroscopic quantities for helping the construction of more accurate multi-temperature model. Nonetheless, it should be noted that full-dimensional PESs for certain air-species collisions are still unavailable and the computational time required for direct molecular simulations is substantial.

The comprehension of the thermochemical nonequilibrium effects (at the molecular level) is experiencing notable advancement thanks to these high-fidelity StS simulations. However, the computational cost rises significantly as the gas mixture incorporates more species and their internal energy states. While recent endeavors have employed the vibrational StS kinetics in two-dimensional hypersonic flows for spheres[27] and double-cones,[31] extending its application to more complex geometries remains challenging. In efforts to mitigate computational cost while preserving the fidelity of the StS model, reduced-order models (ROMs) have been previously introduced in the literature.[8,9,32–35] One of the effective ROMs is the coarse-grained model (CGM),[33,35–39] which lumps the internal energy states with similar characteristics into distinct groups (or called bins), thereby transforming the StS simulation into a group-to-group simulation and making it more like a macroscopic model. Liu *et al.*[33,36] introduced the principle of maximum entropy into CGM, i.e., the logarithm of the distribution function in each group is defined as a polynomial function of internal energy. Their CGM results with only two divided groups can reproduce the vibrational–rotational StS results of macroscopic quantities on the nitrogen gas mixture undergoing internal excitation and dissociation, while recovering the microscopic internal energy distribution should use more than five divided groups. Note that the CGM's accuracy mainly depends on the number of divided groups, the grouping strategy (e.g., energy-based grouping or vibration-based grouping[38]), and the presumed polynomial function of internal energy states.[40] For the vibrational StS modeling, previous studies have used CGM to reproduce the StS results by characterizing the distinct features of the low-lying, medium, and high-lying vibrational states.[41,42] Guy *et al.*[32] developed the nT_v-StSRed model using n groups (each characterized by distinct vibrational temperature) to represent the entire vibrational state space. Recently, Lv *et al.*[35] found that the CGM's accuracy is related to the accuracy of the predicted number densities of groups and developed the CG2T model based on the coarse-grained treatment of molecular vibrational states by proposing an analytical distribution function of vibrational groups, and their results reproduced the StS results for the post-shock oxygen flows with varying degrees of thermochemical nonequilibrium. In addition, recent works have combined CGM with the neural operators to improve the computational efficiency of CGM further while ensuring the underlying physics.[39,43] However, CGM has seldomly been applied to multi-species (more than one diatom) air flows in the literature, so this paper aims to assess its efficacy in simulating high-enthalpy five-species air flows based on the newly updated vibrational StS kinetic mechanism and examine the minimum number of divided groups that can accurately reproduce the StS results. Note that as a limiting case of CGM, lumping all vibrational energy levels into a single bin for each diatom corresponds to the macroscopic multi-vibrational temperature model (characterized by the separate vibrational temperatures of N_2, O_2, and NO[44]), the difference is that by using the coarse-grained treatment, one still uses the high-fidelity StS kinetics.

The remainder of this paper is organized as follows: Section II describes the theories and governing equations of the StS and CGMs; Sec. III reports the details of the newly updated vibrational StS kinetic mechanism; Sec. IV presents comparisons of the StS and CGM (with different numbers of divided groups) results for the post-shock high-enthalpy five-species air flows with varying degrees of thermochemical nonequilibrium and provides a detailed analysis of the performance of different CGMs and the source term evolution behind shock wave; concluding remarks are summarized in the last section.

II. PHYSICAL MODELS

This section introduces the governing equations associated with the StS and CGMs for calculating the post-shock thermochemical nonequilibrium air flows. Five neutral species of air mixture $N_2/O_2/NO/N/O$ on their ground electronic states are considered in the kinetic mechanism. The rotational temperature in the gas mixture is assumed to be equal to the translational temperature since the energy transfer between these two modes is usually efficient. Moreover, a vibrational state-specific description, considering the StS vibrational–chemical kinetics, is applied to diatoms instead of using the vibrational mode approximation.

A. State-to-state model

To accurately describe the vibrational distribution functions (VDFs) of diatoms, the vibrational StS model treats the full vibrational states as pseudospecies and considers the state-specific inelastic and reactive collisions. For the post-shock air flows, the governing equations of the StS model are described by the stationary one-dimensional Euler equations as follows:

$$\begin{cases} \dfrac{d}{dx}(\rho_{c,i}u) = \omega_{c,i}, \\ \dfrac{d}{dx}(\rho u^2 + p) = 0, \\ \dfrac{d}{dx}\left[\rho u\left(h + \dfrac{u^2}{2}\right)\right] = 0, \end{cases} \tag{1}$$

where u, ρ, p, and h represent the gas mixture's velocity, density, pressure, and total enthalpy, respectively, and x is the position coordinate behind the normal shock wave. $\rho_{c,i}$ and $\omega_{c,i}$ are the density and mass production rate of species (component) c at the ith vibrational level, respectively. Specifically, the enthalpy h in Eq. (1) is defined as follows:

$$h = \frac{p}{\rho} + \sum_{c\in \text{atom}} y_c\left(\frac{3}{2}R_cT + h_{0,c}\right) + \sum_{c\in \text{diatom}}\sum_{i\in c} y_{c,i}\left(\frac{5}{2}R_cT + e_{c,i} + h_{0,c}\right), \tag{2}$$

where $h_{0,c}$, R_c, and y_c are the enthalpy of formation, gas constant, and mass fraction of species c, respectively. The term $e_{c,i} = \varepsilon_{c,i}/m_c$, in which m_c is the mass of species c and $\varepsilon_{c,i}$ is the vibrational energy of species c in the ith state. Since the species are assumed to be in their ground electronic states, the electronic energy is not included in this formula. It is important to note that in shock tube experiments, particularly for incident shock wave flows where the core flow remains inviscid and viscous effects are limited to a thin boundary layer, the one-dimensional Euler equations, Eq. (1), provide a good approximation for reproducing experimental data.

The vibrational energy levels of N_2, O_2, and NO are provided in the Appendix. The expression for $\omega_{c,i}$ is derived according to the StS kinetic mechanism. Specifically, this paper considers the StS elementary reactions including VT, VVT, dissociation–recombination (DR), and ZE processes for five-species air flows. The VT energy transfer represents

$$A_{ci} + A_{dk} \rightleftharpoons A_{ci'} + A_{dk}, \tag{3}$$

where A_{ci} represents the molecular formula of species c at the ith vibrational level. For atoms, A_{ci} simplifies to A_c. The V–T process describes the exchange between the vibrational energy of one molecule and the translational energy, while the V–V–T energy transfer refers to

$$A_{ci} + A_{dk} \rightleftharpoons A_{ci'} + A_{dk'}, \tag{4}$$

in which vibrational energies of both molecules participate in the energy exchange process. Moreover, the DR process denotes

$$A_{ci} + A_{dk} \rightleftharpoons A_{c'} + A_{f'} + A_{dk}, \tag{5}$$

where the forward direction is dissociation, while the reverse direction is recombination. $A_{c'}$ and $A_{f'}$ are the products of A_{ci} dissociation. Finally, the ZE process is

$$A_{ci} + A_{dk} \rightleftharpoons A_{c'i'} + A_{d'k'}, \tag{6}$$

in which the atom exchange event happens.

Therefore, the expression of $\omega_{c,i}$ can be readily obtained as follows:

$$\omega_{c,i} = \omega_{c,i}^{vib} + \omega_{c,i}^{DR} + \omega_{c,i}^{ZE}, \tag{7}$$

where $\omega_{c,i}^{vib}$, $\omega_{c,i}^{DR}$, and $\omega_{c,i}^{ZE}$ represent the mass production rates of the inelastic (VT + VVT), DR, and ZE processes, respectively, namely,

$$\begin{aligned} \omega_{c,i}^{vib} &= \sum_{dki'k'} \left(n_{ci'} n_{dk'} k_{c,i'i}^{d,k'k} - n_{ci} n_{dk} k_{c,ii'}^{d,kk'} \right), \\ \omega_{c,i}^{DR} &= \sum_{dk} n_{dk} \left(n_{c'} n_{f'} k_{rec,ci}^{dk} - n_{ci} k_{dis,ci}^{dk} \right), \\ \omega_{c,i}^{ZE} &= \sum_{dc'd'} \sum_{ki'k'} \left(n_{c'i'} n_{d'k'} k_{c'i',ci}^{d'k',dk} - n_{ci} n_{dk} k_{ci,c'i'}^{dk,d'k'} \right), \end{aligned} \tag{8}$$

where n_{ci} is the number density of species c at the ith vibrational level, and $k_{c,ii'}^{d,kk'}$, $k_{dis,ci}^{dk}$, and $k_{ci,c'i'}^{dk,d'k'}$ are the forward rate coefficients of processes (3) [and (4)], (5), and (6), respectively. The backward rate coefficients $k_{c,i'i}^{d,k'k}$, $k_{rec,ci}^{dk}$, and $k_{c'i',ci}^{d'k',dk}$ are related to the forward rate coefficients by the detailed balance principle.[28] The details of the considered elementary reactions and the corresponding rate coefficients in the updated database are described in Sec. III.

B. Coarse-grained model

Grouping energy levels with similar behavior is physically reasonable and has been proven effective in reproducing full StS results.[33,35,37] The intuitive and physically interpretable grouping strategy is the uniform width energy-based grouping[35,38] by lumping the states with close energies, as adjacent energy levels have similar relaxation time scales and efficient energy transfer between them. Although more effective data-driven grouping strategies exist (such as the machine learning framework developed by Jacobsen *et al.*,[45] which utilizes rate-distortion theory to optimize cluster assignments and improve the coarse-grained process in vibrational–rotational StS calculations), the energy-based grouping method used in this work still yields satisfactory results for the cases of interest (see below), when compared to vibrational-specific StS calculations. Specifically, for species c with dissociation energy $D_{0,c}$, each vibrational group G_i contains the vibrational energy levels spanning the energy of $\Delta E = D_{0,c}/N_{g,c}$ if the number of grouping is $N_{g,c}$. The reconstruction of energy level distribution within each group follows the maximum entropy principle[46] (ensuring that the distribution maximizes entropy after molecular collision), i.e.,

$$\ln\left(n_{c,v}^{G_i}\right) = \alpha_c^{G_i} + \beta_c^{G_i} \varepsilon_{c,v} + \cdots, \quad v \in G_i, \tag{9}$$

where $\varepsilon_{c,v}$ is the vibration energy of level v (belonging to group G_i of species c), whose number density is $n_{c,v}^{G_i}$. Note that in this paper, we truncate the above function at the first-order term (linear model) since including higher-order terms needs higher moment closure constraints. The parameters $\alpha_c^{G_i}$ and $\beta_c^{G_i}$ are constrained by taking the moment of the vibration energy of levels within group G_i,[47] and the zero-order moment gives the number density of group G_i, while the first-order moment is the average vibrational energy of group G_i, namely,

$$\sum_{v \in G_i} n_{c,v}^{G_i} = n_c^{G_i}, \quad \sum_{v \in G_i} n_{c,v}^{G_i} \varepsilon_{c,v} = n_c^{G_i} \varepsilon_c^{G_i}, \tag{10}$$

where $n_c^{G_i}$ and $\varepsilon_c^{G_i}$ are the number density and vibration energy of group G_i of species c, respectively. Thus,

$$\alpha_c^{G_i} = \ln\left(\frac{n_c^{G_i}}{Q_c^{G_i}}\right), \quad Q_c^{G_i} = \sum_{v \in G_i} \exp\left(\beta_c^{G_i} \varepsilon_{c,v}\right). \tag{11}$$

If we further define the characteristic temperature for each group as

$$T_v^{G_i} = -\frac{1}{k_B \beta_c^{G_i}}, \tag{12}$$

where k_B is the Boltzmann constant, then, $n_{c,v}^{G_i}$ [namely, Eq. (9)] can readily be expressed as

$$n_{c,v}^{G_i} = \frac{n_c^{G_i}}{Q_c^{G_i}} \exp\left(-\frac{\varepsilon_{c,v}}{k_B T_v^{G_i}}\right). \tag{13}$$

This formula indicates that, under the maximum entropy linear model, the vibrational level distribution within each group is described by the Boltzmann distribution controlled by $T_v^{G_i}$. As energy transfer between adjacent levels is efficient, the accuracy of this linear distribution within each group improves with an increasing number of grouping. When the gas system is in thermal equilibrium ($T = T_v^{G_i}$), the molecular VDF retains the Boltzmann distribution. Moreover, the temperature $T_v^{G_i}$ of each group is solved iteratively by the Newton method according to the first-order moment constraint in Eq. (10).

Therefore, for the post-shock air flows, the governing equations of CGM can be expressed as

$$\begin{cases} \dfrac{d}{dx}\left(\rho_c^{G_i} u\right) = \omega_c^{G_i}, \\ \dfrac{d}{dx}\left(\rho_c^{G_i} u e_c^{G_i}\right) = \omega_{c,vib}^{G_i}, \\ \dfrac{d}{dx}\left(\rho u^2 + p\right) = 0, \\ \dfrac{d}{dx}\left[\rho u \left(h + \dfrac{u^2}{2}\right)\right] = 0, \end{cases} \tag{14}$$

where $e_c^{G_i} = \varepsilon_c^{G_i}/m_c$. It is seen that CGM introduces the dynamical equations for different-order moments of vibrational energy beyond those of the conserved mass, momentum, and total energy. The number of governing equations to be solved is then significantly reduced compared to the StS equations [Eq. (10)]. $\omega_c^{G_i}$ and $\omega_{c,vib}^{G_i}$ are the mass production rate and vibrational energy source term, respectively, for group G_i of species c, i.e.,

$$\omega_c^{G_i} = \sum_{v \in G_i} \omega_{c,v}, \omega_{c,vib}^{G_i} = \sum_{v \in G_i} \varepsilon_{c,v} \cdot \omega_{c,v}. \tag{15}$$

The detailed expressions of these source terms are obtained by taking (zero-order and first-order) moments of the vibrational energy in Eq. (7) and summing over vibrational states within group G_i. Note that the same state-specific kinetic mechanism as the StS model is adopted so that the cost of computing the source terms is not reduced in CGM (except for directly obtaining the group-specific rate coefficients using molecular dynamic simulation[38] or using the neural network regression[35]). Furthermore, in solving the governing equations for the StS and CGMs, namely, Eqs. (1) and (14), respectively, the post-shock values are derived from the Rankine–Hugoniot relations, assuming that vibrational modes and gas composition remain frozen across the shock wave, and the equations are numerically solved using the fourth-order Runge–Kutta method.

III. THE UPDATED StS KINETIC MECHANISM

Although *ab initio* calculations and experimental measurements can provide the highest-fidelity state-specific rate coefficients for air species, these data are often unavailable or complete and instead necessitate using (semi)empirical methods. By summarizing the available state-specific rate coefficients (combining data from *ab initio* calculations and the FHO model) of five-species air mixture $N_2(v)/O_2(v)/NO(v)/N/O$ in 2012, Da Silva *et al.*[19] developed the open-source STELLAR database. However, the STELLAR database simplifies the VVT energy exchange processes in the diatom–diatom collisions to VT processes and omits some StS processes (such as the VT transition of the O_2–N collision and certain reactions involving NO, etc.). Since then, many *ab initio* calculations have been performed for collisions between air species. Therefore, we develop and distribute in this paper a more comprehensive vibrational state-specific dataset for the five-species air mixture based on the data that reflect the state-of-the-art. The considered elementary reactions include the type of the VVT, VT, DR, and ZE processes, which are summarized in Table I along with the methods adopted to calculate the rate coefficients. The presently released version does not consider the ionized species and the associated reactions. For reactions lacking available *ab initio* calculations, we supplement with the *ad hoc* data obtained by semiempirical models. The number of vibrational energy levels in the ground electronic state of N_2 is 55 (detailed energy levels are reported in Table A1), which is adopted from Fangman and Andrienko[48] by solving the one-dimensional radial Schrödinger equation based on the diatomic potential energy curve of N_2 in the Minnesota N_4 ground PES.[49] The number of N_2 vibrational ladder 55 is also obtained in Ref. 22 by using the LEVEL16 program. Moreover, the vibrational energy levels in the ground electronic state of O_2 and NO are 46 and 48 (see Table V), respectively, as determined by Lopez and Lino Da Silva[28] by solving the radial Schrödinger equation based on the potential energy curves reconstructed using the semi-classical Rydbert–Kelin–Rees method. Unlike the commonly used Dunham expansion extrapolation, these *ab initio* calculated vibrational ladders provide a more accurate description of intermediate and high-lying vibrational energy levels.

A. Vibrational–vibrational–translational (VVT) energy exchange processes

The data of vibrational inelastic VVT rate coefficients for diatom–diatom collisions (specifically, N_2–O_2, N_2–NO, O_2–NO, and O_2–O_2 collisions) are calculated in this paper using the FHO model. The FHO model is a semi-classical non-perturbative approach to efficiently obtain the VVT and VT transition probabilities (and rate coefficients) for a harmonic oscillator influenced by an external analytical force field.[54–56] The original derivation was made on assuming collinear collision,[54] and later improved modifications were incorporated to account for anharmonicity, steric factors, and detailed balance.[55] Specifically, the expression of the FHO model for

TABLE I. Vibrational state-specific kinetic mechanism for the five-species non-ionized air gas mixture.

No.	Type	Reaction	Model	References
1	VVT	$N_2(i) + O_2(k) = N_2(i') + O_2(k')$	FHO	This paper
2	VVT	$N_2(i) + NO(k) = N_2(i') + NO(k')$	FHO	This paper
3	VVT	$O_2(i) + NO(k) = O_2(i') + NO(k')$	FHO	This paper
4	VVT	$O_2(i) + O_2(k) = O_2(i') + O_2(k')$	FHO	This paper
5	VT	$N_2(i) + M = N_2(i') + M, M = N_2,\ N$	QCT	48
6	VT	$N_2(i) + O = N_2(i') + O$	QCT	23
7	VT	$O_2(i) + N = O_2(i') + N$	QCT	24
8	VT	$O_2(i) + O = O_2(i') + O$	QCT (STELLAR)	15 and 19
9	VT	$NO(i) + M = NO(i') + M, M = NO, N, O$	FHO	This paper
10	DR	$N_2(i) + M = N + N + M, M = N_2,\ N$	QCT	48
11	DR	$N_2(i) + O = N + N + O$	QCT	23
12	DR	$O_2(i) + N = O + O + N$	QCT	24
13	DR	$O_2(i) + O = O + O + O$	QCT (STELLAR)	15 and 19
14	DR	$O_2(i) + O_2 = O + O + O_2$	FHO (STELLAR)	19
15	DR	$N_2(i) + O_2 = N + N + O_2$	MT $(k_{dis})^{eq}$ from Ref. 8	This paper
16	DR	$O_2(i) + N_2 = O + O + N_2$	MT $(k_{dis})^{eq}$ from Ref. 50	This paper
17	DR	$NO(i) + N_2 = N + O + N_2$	MT $(k_{dis})^{eq}$ from Refs. 51 and 3	This paper
18	DR	$N_2(i) + NO = N + N + NO$	MT $(k_{dis})^{eq}$ from Ref. 52	This paper
19	DR	$O_2(i) + NO = O + O + NO$	MT $(k_{dis})^{eq}$ from Ref. 52	This paper
20	DR	$NO(i) + M = N + O + M, M = O_2, NO, N, O$	MT $(k_{dis})^{eq}$ from Ref. 53	This paper
21	ZE	$N_2(i) + O = NO(i') + N$	QCT	23
22	ZE	$O_2(i) + N = NO(i') + O$	QCT	24

the transition probability of the VVT process $A_{ci} + A_{dk} \rightleftharpoons A_{ci'} + A_{dk'}$ is derived by Zelechow *et al.*[54] as follows:

$$\begin{aligned} &P(i,k \to i',k',\varepsilon,\rho) \\ &\quad = \Bigg| \sum_{r=0}^{n} (-1)^{i_{12}-r} C^{i_{12}}_{r+1,k+1} C^{f_{12}}_{r+1,k'+1} \times \varepsilon^{\frac{1}{2}(i_{12}+f_{12}-2r)} \\ &\qquad \times \exp\left(-\frac{\varepsilon}{2}\right) \sqrt{(i_{12}-r)!(f_{12}-r)!} \\ &\qquad \times \exp[-j(f_{12}-r)\rho] \sum_{l=0}^{n-r} \frac{(-1)^l}{l!(i_{12}-r-l)!(f_{12}-r-l)!} \frac{1}{\varepsilon^l} \Bigg|^2, \end{aligned} \tag{16}$$

where j denotes complex number, $i_{12} = i + k$, $f_{12} = i' + k'$, $n = \min(i_{12}, f_{12})$, and $C^k_{i,j}$ is the transformation matrix as follows:

$$C^k_{i,j} = 2^{-\frac{k}{2}} \binom{k}{i-1}^{\frac{1}{2}} \binom{k}{j-1}^{-\frac{1}{2}} \sum_{\nu=0}^{j-1} (-1)^{\nu} \binom{k-i+1}{j-\nu-1} \binom{i-1}{\nu}, \tag{17}$$

in which $\binom{i}{j}$ is the binomial coefficient. Moreover, ε and ρ are related to the transition probability obtained by the first-order perturbation theory. When assuming that the interaction potential energy is a pure repulsive potential [namely, $V(R) \sim \exp(-\alpha R)$, and R is the intermolecular distance], the analytic solutions for ε and ρ are[54]

$$\begin{aligned} \varepsilon &= S_{VT} \frac{8\pi^3 \omega (\tilde{m}^2/\mu) \gamma^2}{\alpha^2 h} \sinh^{-2}\left(\frac{\pi\omega}{\alpha\bar{v}}\right), \\ \rho &= \sqrt{S_{VV}} (2\tilde{m}^2/\mu) \gamma^2 \alpha \bar{v}/\omega, \end{aligned} \tag{18}$$

where h is the Planck constant, ω denotes the oscillator frequency, $\bar{v}$ is the average collision velocity, and μ, γ, and $\tilde{m}$ are the mass parameters. The detailed expressions of these parameters are referred to Refs. 55 and 56. S_{VT} and $\sqrt{S_{VV}}$ are the steric factors that generalize the assumption of collinear collision to the general case of noncollinear collision.

The rate coefficient is obtained by considering a one-dimensional Maxwellian distribution of the relative collision velocity of particles and multiplying the averaging transition probability by the gas-kinetic collision frequency, namely,

$$k^{d,kk'}_{c,ii'}(T) = \sigma \sqrt{\frac{8k_B T}{\pi \tilde{m}}} \left(\frac{\tilde{m}}{k_B T}\right) \int_0^{\infty} P(i,k \to i',k') \cdot \exp\left(\frac{-\tilde{m}v^2}{2k_B T}\right) \cdot v dv, \tag{19}$$

where v is the relative collision velocity and σ is the collisional cross section.

The VVT rate coefficients for processes 1–4 in Table I are obtained by Eq. (19) for the temperature range of 100–25 000 K (only exothermic processes are explicitly computed, while the endothermic ones are obtained by the detailed balance principle). The adopted FHO parameters are taken from Ref. 56: $\sigma = 40$ Å^2, $\alpha = 4$ Å^{-1}, $S_{VT} = 4/9$, and $S_{VV} = 1/27$ (except that $\alpha = 4.2$ Å^{-1} for process 4 in Table I). For these VVT processes, the allowed quantum transition number is limited to 5 (namely, $\Delta i \leq 5$ and $\Delta k \leq 5$) to reduce the computational cost in the subsequent StS and CGM calculations using these data, and the rate coefficients for $\Delta i > 5$ or $\Delta k > 5$ are generally small enough.

Figure 1 shows the rate coefficients of VT and VVT processes for selected $O_2 + O_2$ and $N_2 + O_2$ collisions. It is seen in Fig. 1(a) that the present FHO results for the single-quantum VT transition of $O_2(1) + O_2(0)$ and $O_2(10) + O_2(0)$ collisions are in good agreement with the mixed quantum-classical (MQC) calculations (based on a spin-averaged $O_2 + O_2$ PES) by Hong *et al.*[21] and experimental data[57] except for very low temperatures. Moreover, the rate coefficients for the VT processes are several orders of magnitude lower than the VVT processes with the same initial vibrational states at lower temperatures (below 3000 K). As temperature increases, the VT efficiency rapidly grows, and its rates surpass those of VVT at higher temperatures. Figure 1(b) presents the VT and VVT rate coefficients for $O_2(i) + O_2(0)$ collisions up to $i = 30$. The present FHO results show good agreement with the MQC results by Hong *et al.*[21] for near-resonant VVT processes $O_2(i) + O_2(0) \to O_2(i-1) + O_2(1)$ for $T = 1000$ K (where the VVT process dominates) and single-quantum VT processes $O_2(i) + O_2(0) \to O_2(i-1) + O_2(0)$ for $T = 5000$ K (the largest temperature where MQC data are available). Figure 1(c) shows the VT rate and VVT rate coefficients of $N_2(1) + O_2(0)$ collisions. The FHO rate coefficients for the VVT process $N_2(1) + O_2(0) \to N_2(0) + O_2(1)$ agree well with the experimental data[58] (which, however, might have considerable uncertainty, as analyzed by Andrienko and Boyd[50]), while they are much larger than the MQC results by Garcia *et al.*[59] and QCT results by Andrienko and Boyd,[50] especially at lower temperatures. This disagreement between the molecular dynamical results (MQC and QCT) and the experimental data may be attributed to some uncertainties in the adopted PES[50] or in the experimental measurement. Similarly, the FHO rate coefficients for the VT process $N_2(1) + O_2(0) \to N_2(0) + O_2(0)$ are larger than the MQC[59] and QCT[50] results. Below 3000 K, the QCT results strongly underestimate the rate coefficients due to its failure to capture the influence of quantum effects at low temperatures. In general, the FHO model not only can obtain the rate coefficient dataset efficiently using only several model parameters but also gives VT and VVT rate coefficients (for processes 1–4 in Table I) that agree reasonably well with the MQC calculations and experimental data.

B. Vibrational–translational (VT) energy transfer processes

The present data of vibrational inelastic VT rate coefficients for diatom–atom collisions (processes 5–8 in Table I) are taken from the QCT calculations in the literature. Specifically, the VT rate coefficients for N_2–N collisions are obtained by the regression formulas, proposed by Fangman and Andrienko,[48] fitting to the QCT calculations (in the range of temperatures between 5000 and 30 000 K) based on the Minnesota N_4 ground PES with one nitrogen atom displaced to infinity.[49] For the VT rate coefficients of N_2–O and O_2–N collisions, we adopt the interpolation formulas proposed by Esposito and Armenise[23,24] based on the QCT calculations (in the range of temperatures between 1000 and 20 000 K) using the $^3A''$ and $^3A'$ PESs for the N_2–O system and $^2A'$ and $^4A'$ PESs for the O_2–N system, respectively. Moreover, for the O_2–O collisions, the VT rate coefficients are taken from the collected dataset in the STELLAR database and are based on the QCT calculations (in the range of temperatures between 50 and 10 000 K) made by Esposito *et al.*[15] For the NO–O and NO–N collisions, to our knowledge, there are no available VT rate coefficient datasets from *ab initio* calculations, so we use the aforementioned FHO

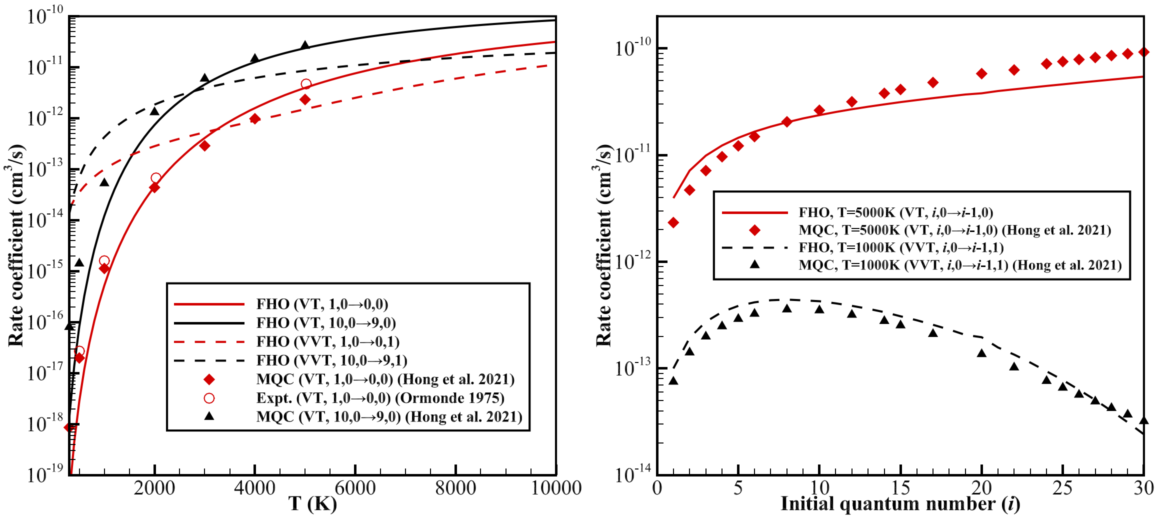

(a) $O_2(1)$+$O_2(0)$ and $O_2(10)$+$O_2(0)$ collisions (b) $O_2(i)$+$O_2(0)$ collisions

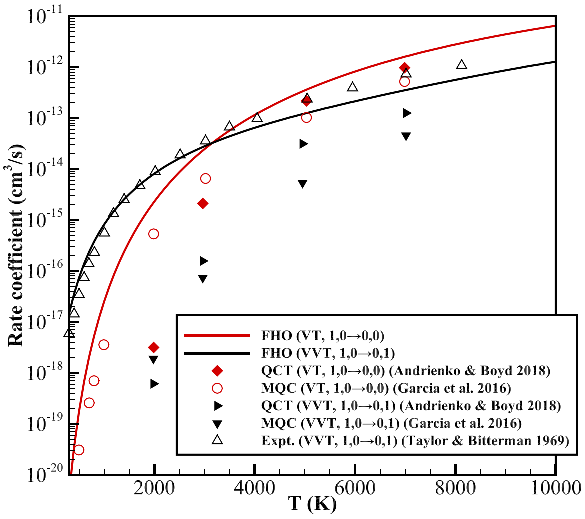

(c) $N_2(1)$+$O_2(0)$ collisions

FIG. 1. Rate coefficients for VT and VVT processes of selected $O_2 + O_2$ and $N_2 + O_2$ collisions.

model to obtain the data for the full vibrational ladder of NO. Note that the VVT processes of the NO–NO collisions are reduced to VT processes for simplicity and also calculated using the FHO model, as the NO–NO collisions are affected by the nonadiabatic electronic transitions and lack *ab initio* calculations or experimental data for validation. The expression of the FHO model for the transition probability of the VT process $A_{ci} + A_d \rightleftharpoons A_{ci'} + A_d$ of diatom–atom collisions is[60]

$$P(i \to i', \varepsilon) = i!i'!\varepsilon^{i+i'} \exp(-\varepsilon) \left| \sum_{r=0}^{n} \frac{(-1)^r}{r!(i-r)!(i'-r)!} \frac{1}{\varepsilon^r} \right|^2, \quad (20)$$

where $n = \min(i, i')$, and ε has the same expression as in Eq. (18). The adopted parameters σ, α, and S_{VT} are taken from the values used by Oblapenko[61] for the NO-related collisions, and the VT rate coefficients are calculated for the temperature range of 100–25 000 K.

For process 5 in Table I, it should be noted that the QCT inelastic rate coefficients of N_2–N_2 collisions, calculated by Fangman and Andrienko[48] using the Minnesota N_4 singlet PES,[49] are only available for VT processes (assuming one of the N_2 molecules in the vibrational ground state and unchanged after collision). These QCT rate coefficients represent the state-of-the-art for high temperatures and provide the state-specific data for the whole vibrational ladder of N_2. Figure 2(a) shows the above QCT rate coefficients for $N_2(1) + N_2$ and $N_2(20) + N_2$ single-quantum VT transitions as a function of temperature. It is seen that the present adopted QCT fitting formulas are lower than the FHO results from the STELLAR database[19] except for the

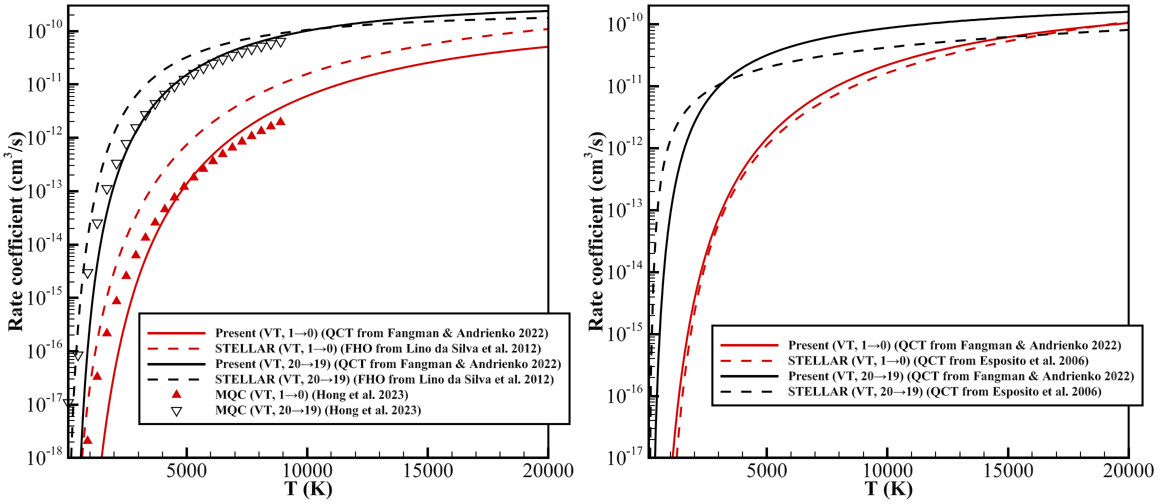

(a) $N_2(i)$+N_2 → $N_2(k)$+N_2 collisions

(b) $N_2(i)$+N → $N_2(k)$+N collisions

FIG. 2. Rate coefficients for VT processes of selected $N_2 + N_2$ and $N_2 + N$ collisions.

case of higher vibrational level at high temperatures. The QCT calculations are close to the MQC calculations by Hong *et al.*[22] for the temperature range of 4000–9000 K, while for the lower temperatures, QCT data (note that the formulas were fitted to the QCT calculations in the temperatures between 5000 and 30 000 K[48]) strongly underestimate the rate coefficients since the method fails to capture the relevant quantum effects. The comparisons also apply to $N_2(i) + N$ single-quantum VT transitions. As depicted in Fig. 2(b), the QCT fitting formula proposed by Fangman and Andrienko[48] aligns well with the QCT data calculated by Esposito *et al.*[16] (collected in the STELLAR database) for the $N_2(1) + N$ VT relaxation. The influence of different adopted PESs in the above two QCT calculations is small for lower vibrational states, but a significant distinction is observed for the $N_2(20) + N$ collision. Note that the PES adopted in Fangman and Andrienko's QCT calculations was developed more recently based on higher level *ab initio* points and gives 55 states in the vibrational ladder of N_2,[48] differing from the value of 68 obtained by Esposito *et al.*[16] based on an older PES.

The isothermal heat baths of nitrogen mixture (three separate cases with $T = 8000$, 12 000, and 20 000 K) reported in Ref. 48 are computed using the StS model to investigate the influence of different rate coefficient datasets. The vibrational temperature is initialized at 300 K, and only diatomic nitrogen exists initially with $n_{N_2} = 10^{25}\ \mathrm{m}^{-3}$. Both VT and DR (see Sec. III C) processes of $N_2(i) + N$ and $N_2(i) + N_2$ collisions are considered. The vibration temperature of diatomic species c, $T_{v,c}$, is defined as

$$\sum_i \frac{n_{c,i}}{n_c}\varepsilon_{c,i} = \frac{\sum_i \varepsilon_{c,i}\exp\left(-\frac{\varepsilon_{c,i}}{k_B T_{v,c}}\right)}{\sum_i \exp\left(-\frac{\varepsilon_{c,i}}{k_B T_{v,c}}\right)}. \tag{21}$$

Figure 3 shows the vibrational temperatures of N_2 in three isothermal heat baths. The vibrational temperature increases due to VT transitions and gradually reaches the equilibrium isothermal temperature. The differences between the StS results using two different datasets of $N_2(i) + N$ and $N_2(i) + N_2$ collisions are significant. For the cases of $T = 8000$ and 12 000 K, the results obtained using the STELLAR dataset exhibit a considerably shorter vibrational relaxation time than those obtained from Fangman and Andrienko.[48] This difference is explained in Fig. 2(a), where the VT rate coefficients of $N_2(i) + N_2$ collisions, dominant in the initial relaxation phase, are much larger in the STELLAR dataset. For $T = 20\,000$ K, a quasi-steady-state region is visible, as indicated by the plateau before the equilibrium state, where thermalization of the vibrational mode is not yet completed and

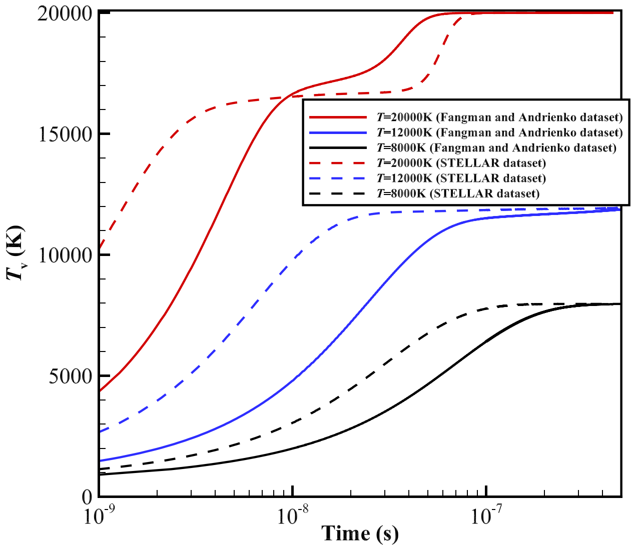

FIG. 3. Vibrational temperatures in isothermal heat baths. Solid and dashed lines are the StS results obtained using the different datasets of $N_2(i) + N$ and $N_2(i) + N_2$ collisions from Fangman and Andrienko[48] and STELLAR,[19] respectively.

dissociation significantly occurs. Since the result obtained using the STELLAR dataset gives a faster vibrational excitation (promoting dissociation), it leads to an earlier onset of the quasi-steady-state plateau.

Rate coefficients of processes 6, 7, and 9 in Table I are not available in the STELLAR database. Previous works[14,20] supplemented these VT rate coefficients by the classical L–T relaxation model. Specifically, the global behavior of the L–T relaxation is recovered by choosing the state-specific rate coefficient for the VT process $A_{ci} + A_d \rightleftharpoons A_{ci'} + A_d$ as[14]

$$k^d_{c,ii'} = \frac{1}{n_d \tau_{c-d}} \left(\frac{\rho_{c,i'}}{\rho_c}\right)^{eq}, \tag{22}$$

where $\left(\frac{\rho_{c,i'}}{\rho_c}\right)^{eq}$ denotes the VDF at thermal equilibrium and τ_{c-d} is the vibrational relaxation time of species c colliding with species d (composed of the vibrational relaxation time obtained by the Millikan–White formula[62] and the high-temperature collision-limiting correction proposed by Park[3]). Note that the L–T model does not unambiguously specify the state-specific rate coefficients. As a result, the L–T rate coefficient surfaces for N_2 + O and O_2 + N collisions (the number density n_d in Eq. (22) is assumed one half of the total number density composed of the collision partners) at $T = 10\,000$ K shown in Fig. 4 appear as flat planes. Moreover, the L–T rate coefficients are notably different from the QCT calculations conducted by Esposito and Armenise.[23,24] The QCT data clearly demonstrate the state-specific characteristics of the VT transition, illustrating a significant decrease in the transition efficiency as Δi increases. Since the L–T model fails to accurately reflect the state-specific feature of the VT transition, the QCT data and FHO results updated in the present database (Table I) are more appropriate.

C. Dissociation–recombination (DR) processes

The present data of the DR processes 10–13 in Table I are taken from QCT calculations in the literature. Specifically, the dissociation rate coefficients for $N_2(i) + N_2$ and $N_2(i)$ + N collisions are obtained by the regression formulas, proposed by Fangman and Andrienko,[48] fitting to the QCT data (the same calculations for VT processes). For $N_2(i)$–O and $O_2(i)$–N collisions, the dissociation rate coefficients are again taken from the QCT calculations by Esposito and Armenise,[23,24] and the dissociation rate coefficients of $O_2(i)$–O collisions are taken from the QCT calculations made by Esposito *et al.*[15] (collected in the STELLAR database). Additionally, the dissociation rate coefficients of $O_2(i)$–O_2 collisions (process 14 in Table I) are sourced from the STELLAR database and calculated by Da Silva *et al.*[63] using the FHO model. The weighted sum of these state-specific coefficients gives the thermal dissociation rate coefficients[63] that are examined to agree well with the data proposed in popular chemical datasets, stemming mainly from shock-tube experiments conducted at high temperatures.

In the STELLAR database, the dissociation rate coefficients of $N_2(i) + O_2$, $O_2(i) + N_2$, $NO(i) + O_2$, and $NO(i) + N_2$ collisions are also obtained by the FHO model, while the data for the remaining processes are not available. In addition to the FHO model, two other models are commonly used in the literature to obtain the state-specific dissociation rate coefficient: the ladder-climbing model assuming dissociation only from the last vibrational level,[11] which is generally oversimplified, and the MT model proposed by Marrone and Treanor[6] assuming that molecules with higher vibrational energy are more prone to dissociation (preferential dissociation). Specifically, the MT model redistributes the state-specific rate coefficients from the thermal equilibrium dissociation rate coefficient, $(k^{dk}_{dis,ci})^{eq}$, for process $A_{ci} + A_{dk} \rightleftharpoons A_{c'} + A_{f'} + A_{dk}$ as follows:

$$k^{dk}_{dis,ci} = Z(i) \cdot \left(k^{dk}_{dis,ci}\right)^{eq} = Z(i) \cdot C_f T^{\eta_f} \exp\left(-\frac{\theta_f}{T}\right), \tag{23}$$

where C_f, η_f, and θ_f are the Arrhenius parameters. Moreover, $Z(i)$ is the nonequilibrium factor

$$Z(i) = \frac{Q_{vib}(T)}{Q_{vib}(-U)} \exp\left[\frac{\varepsilon_{c,i}}{k_B}\left(\frac{1}{T} + \frac{1}{U}\right)\right], \tag{24}$$

where Q_{vib} is the equilibrium vibrational partition function, and the parameter U has the dimension of temperature and describes how the

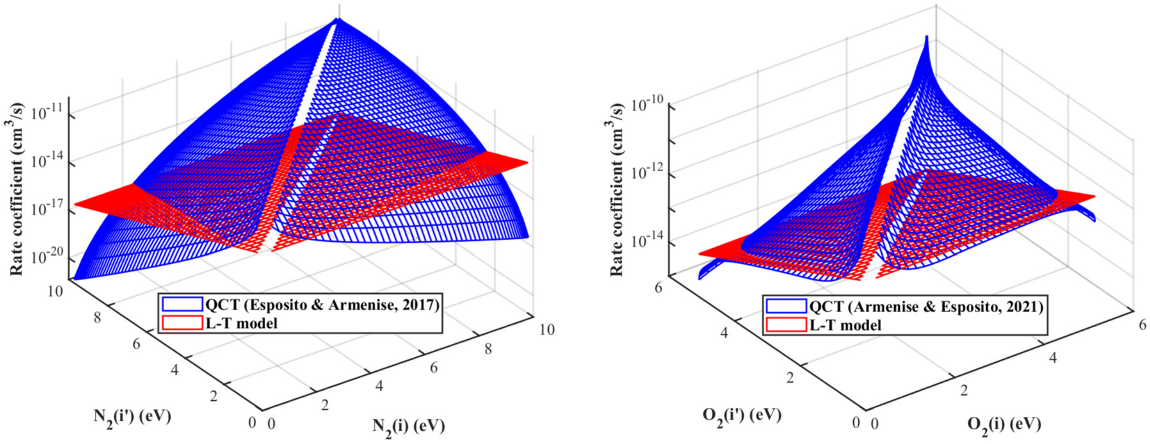

(a) $N_2(i)$+O↔$N_2(i')$+O

(b) $O_2(i)$+N↔$O_2(i')$+N

FIG. 4. Comparisons of VT rate coefficients for N_2 + O and O_2 + N collisions obtained by QCT calculations and L–T model, respectively, at $T = 10\,000$ K.

probability of the reaction increases with the increase in vibrational energy. Herein, U is set to 1/3 of the dissociation characteristic temperature of species c. Furthermore, the state-specific recombination rate coefficients are computed from the detailed balance principle.

Figure 5(a) shows the adopted QCT rate coefficients for $N_2(i)$ + N dissociation from Fangman and Andrienko,[48] and the corresponding data in the STELLAR database (taken from the QCT calculations by Esposito *et al.*[16]) generally agree well with these data within the order of magnitude. Dissociation increases with temperature and vibrational energy, and dissociation from very low vibrational levels becomes substantial for very high gas temperatures. Figure 5(b) compares the adopted QCT rate coefficients[48] and the FHO results (in the STELLAR database) for the $N_2(i) + N_2$ dissociation. An unphysical decrease in the rate coefficient with vibrational energy is observed near the diatomic dissociation limit for the FHO results, deviating from the trend depicted in the trajectory results. This issue is also seen in the FHO results (from the STELLAR database) in Figs. 5(c)–5(f) for other DR processes. Therefore, the DR rate coefficients of processes 15–20 in Table I are presently calculated within the framework of the MT model. The Arrhenius parameters for $(k^{dk}_{dis,ci})^{eq}$ are reported in Table II. These parameters are chosen from the literature based on QCT calculations[8,50] or data interpreted from experiments.[3,51,52,64] Particularly, as suggested by Kim and Jo,[53] the Arrhenius parameters proposed by Tsang and Herron[64] are employed for NO + O_2, NO + NO, NO + N, and NO + O collisions. Additionally, the thermal equilibrium dissociation rate coefficient for the NO + N_2 collision is determined by combining (using the tanh function) rates below 10 000 K (considering the validity range of experiments), obtained by the Arrhenius parameters suggested in Ref. 51, and rates above 10 000 K, obtained by the Arrhenius parameters suggested in Ref. 3. It is seen in Figs. 5(e) and 5(f) that the MT results for NO dissociation do not have the unphysical peak before the dissociation limit, and their difference with the FHO data is significant for lower temperatures. Future high-fidelity trajectory calculations would help validate these state-specific rate coefficients for NO dissociation.

D. Zeldovich-exchange (ZE) processes

The QCT calculations for ZE processes were conducted by Bose and Candler[17,18] about thirty years ago to investigate the dependency of rate coefficients on the vibrational state of N_2 and O_2 and the product vibrational energy distribution of NO. While Bose and Candler's studies did not offer explicit expressions for explicitly determining the vibrational distributions of the NO products, Da Silva *et al.*[19] assumed a functional form for these distributions based on the above sample QCT data[17,18] at different temperatures. Therefore, the state-specific ZE rate coefficients are available in the STELLAR database.

Recently, Esposito and Armenise[23,24] performed QCT calculations within 1000–20 000 K for O_2–N and N_2–O collisions (we have used their VT and DR rates in Table I) based on updated *ab initio* PESs. These calculations gave fitting formulas for the state-specific rate coefficients of ZE processes as functions of temperature and vibrational energies for both the reagents and products. Since the functions are defined in terms of vibrational energies, interpolating rate coefficients based on energy values (in Appendix A) rather than quantum numbers is straightforward. In Fig. 6, the recent QCT rate coefficients are compared to those from the STELLAR database for N_2 + O and O_2 + N ZE collisions at temperatures of 1000, 10 000, and 20 000 K. For the case of 1000 K [Figs. 6(a) and 6(d)], noticeable threshold behavior of rate coefficient is observed in both two ZE reactions for higher NO (i') states. A peculiar discrepancy is seen in the STELLAR data for $N_2(i) + O \rightarrow NO\ (i') + N$ collisions, which appear several orders of magnitude lower compared to the recent QCT results. In contrast, the data for $O_2(i) + N \rightarrow NO\ (i') + O$ collisions exhibit a closer agreement between the two databases.

At high temperatures of 10 000 and 20 000 K, the rate coefficient profiles for $N_2(i) + O \rightarrow NO\ (i') + N$ collisions [Figs. 6(b) and 6(c)] from both databases exhibit agreement within an order of magnitude and show a much less vibrational bias compared to the lower temperature case. When considering a fixed NO (i') state, there is a trend toward a gradual decrease in the values as vibrational energy increases after reaching a specific maximum value. The rate coefficient profiles for $O_2(i) + N \rightarrow NO\ (i') + O$ collisions [Figs. 6(e) and 6(f)] from the STELLAR database are generally higher than the recent QCT data, and the difference becomes more pronounced as the quantum number i increases. For the very high-lying $O_2(i)$ states, the trends of both databases are opposite. Additionally, the rate coefficient profiles exhibit plateaus, and the length of these plateau regions depends on the specific NO (i') state being considered.

E. StS simulations based on the present state-specific kinetic mechanism

The rate coefficient database of the present state-specific vibrational–chemical kinetic mechanism (Table I) is available in ZENODO.[65] The accuracy of the sub-mechanism for the binary O_2/O mixture was already examined by the authors,[35] showing good agreements between the StS simulations and experimental data. In the following, the full vibrational–chemical kinetic mechanism in Table I is assessed by comparing the StS simulations (considering five-species $N_2/O_2/NO/N/O$) to the shock-tube experiments by Wurster *et al.*[66] (measuring the infrared radiation of the NO molecule) for post-shock reacting air flows. The simulated upstream conditions are shown in Table III (cases 1 and 2), and the upstream gas mixture consisted of nitrogen and oxygen with the Boltzmann vibrational distribution. Specifically, the gas composition is 77.7% N_2 and 22.3% O_2 in case 1 and 60% N_2 and 40% O_2 in case 2.

Figure 7 shows the evolution of the infrared radiation intensity in the 5–5.5 μm NO band, measured experimentally and obtained numerically by the StS simulations based on the present and STELLAR databases, behind the normal shock wave. In the figure, the time is related to the post-shock position by $t = x/U_\infty$. The calculated infrared radiation intensity S is obtained by the semiempirical correlation proposed in Refs. 67 and 68 as follows:

$$S = 1.29 \times 10^{-26} n_{NO} [1 + 1.31 \times 10^{-4}(T - 3000)],\ \mathrm{W}/(\mathrm{m}^3 \cdot \mathrm{sr}), \tag{25}$$

which indicates that the radiation intensity is proportional to both the gas temperature T and the NO number density. The general post-shock relaxation processes of NO molecules are observed in Fig. 8: the translational energy is transferred into the vibrational energies of N_2 and O_2, accompanied by their dissociation; the resulting atoms then initiate ZE reactions that lead to the formation of NO; as NO molecules accumulate, they contribute to reverse ZE reactions and their own dissociation, ultimately stabilizing the number density of NO at

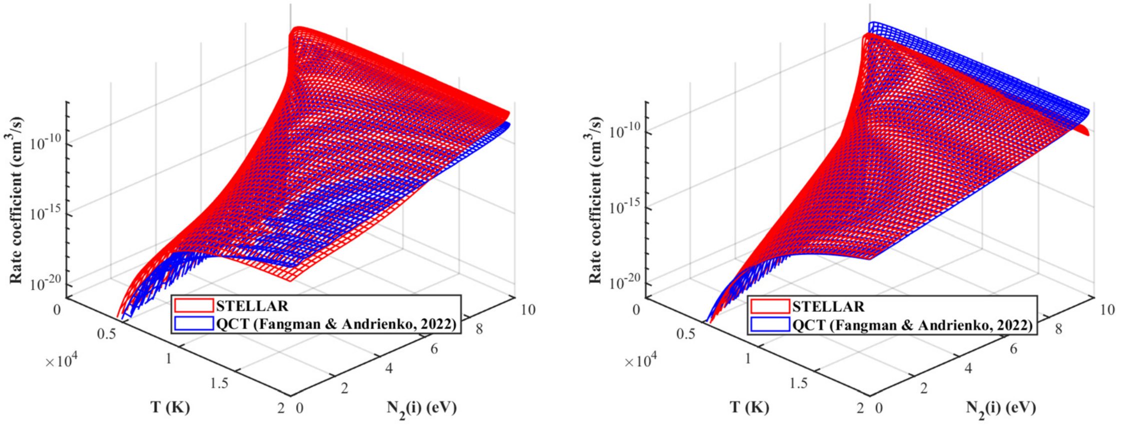

(a) $N_2(i)+N \rightarrow N+N+N$ (b) $N_2(i)+N_2 \rightarrow N+N+N_2$

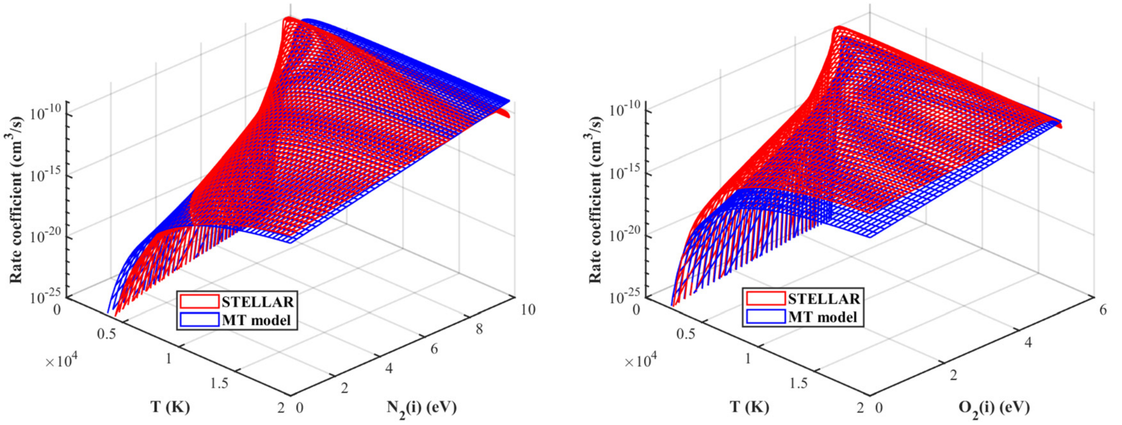

(c) $N_2(i)+O_2 \rightarrow N+N+O_2$ (d) $O_2(i)+N_2 \rightarrow O+O+N_2$

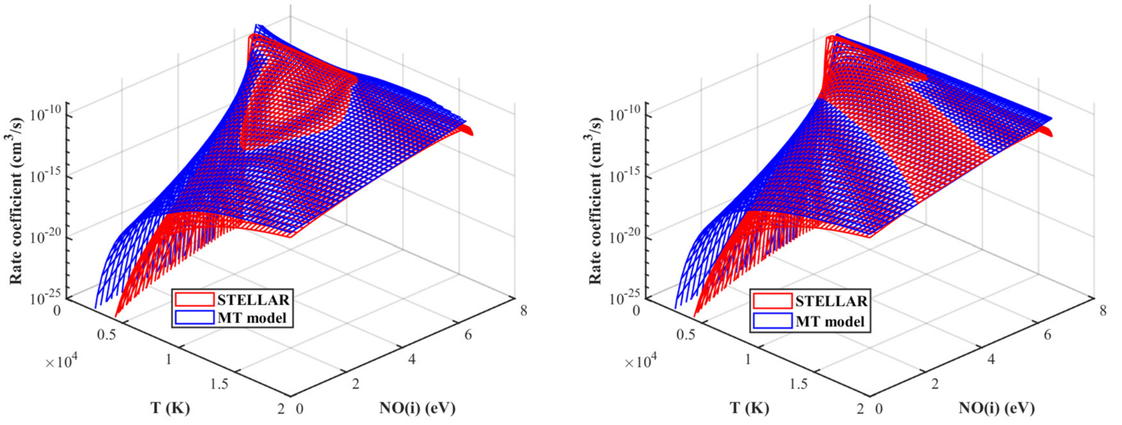

(e) $NO(i)+N_2 \rightarrow N+O+N_2$ (f) $NO(i)+O_2 \rightarrow N+O+O_2$

FIG. 5. Comparisons of dissociation rate coefficients from the present and STELLAR database for selected collisions.

TABLE II. Arrhenius parameters for different systems.

c, i	d, k	$C_f\,(\mathrm{cm^3\ s^{-1}}\ K^{-\eta_f})$	η_f	$\theta_f\,(\mathrm{K})$	References
N_2	O_2	8.3724×10^{-5}	-0.9991	116 892	8
O_2	N_2	8.132×10^{-10}	-0.131	59 380	50
NO	N_2		Combination[a]		3 and 51
N_2	NO	1.16×10^{-2}	-1.6	113 200	52
O_2	NO	5.57×10^{-9}	-0.2726	59 500	52
NO	O_2	2.41×10^{-9}	0	75 200	53
NO	NO, N, O	1.60×10^{-9}	0	75 200	53

[a] The thermal equilibrium dissociation rate coefficient of this collision is obtained by merging (using the tanh function) the parameters proposed in Ref. 51 (for temperatures lower than 10 000 K) and the ones proposed in Ref. 3 (higher than 10 000 K).

its equilibrium value. Note that the vibrational temperature of NO immediately behind the shock is close to the translational temperature, since NO is not present in the upstream flow and formed directly in vibrationally excited states without needing to climb the vibrational ladder.[28] Moreover, the ZE rate coefficients used in the present database lead to a lower NO vibrational temperature than the STELLAR database. Figure 8 also shows that the STELLAR database result gives a more rapid vibrational relaxation of N_2 and O_2 immediately behind the shock (see also Fig. 3). This accelerated relaxation in the STELLAR database result leads to a higher degree of dissociation, which consumes more vibrational energy from N_2 and O_2 (thus lowering the gas temperature T) and generates more NO molecules (the mole fraction of NO reaches its peak earlier but with a lower value). Consequently, for case 1, while both the StS results based on the present database and the STELLAR database accurately reproduce the experimentally measured position of peak radiation intensity, there are notable differences in the peak values. The peak value obtained using the STELLAR database is 25% lower than the experimental data and consistently shows lower radiation intensity after the peak, while the results using the present database agree well with the experimental data, showing only an 8% deviation at the peak value.

For case 2, the results calculated using the present database show good agreement with the experimental data in Fig. 7, although the calculated peak position is slightly delayed. In contrast, the results from the STELLAR database differ significantly from the experimental data. In light of the above results and considering the inclusion of more recent trajectory calculations in the state-specific kinetic mechanism, the present database is expected to provide more accurate predictions for high-temperature five-species air flows.

IV. COARSE-GRAINED SIMULATIONS BASED ON THE UPDATED StS KINETIC DATABASE

Based on the updated StS kinetic database, the effectiveness of the CGMs (with varying numbers of grouping) is assessed for post-shock air flows. Specifically, the CGMs with one to three divided groups (referred to as CGM-1G, CGM-2G, and CGM-3G, respectively) in molecules (N_2, O_2, and NO) are considered, and the division of groups follows the energy-based criterion. For instance in the CGM-3G model, vibrational energy levels of N_2 are lumped into three groups with equal energy (see the Appendix for the detailed energy values): G_1 $(i = 0 - 11)$, G_2 $(i = 12 - 26)$, and G_3 $(i = 27 - 54)$. It should be noted that the CGM-1G model is similar to the macroscopic multi-vibrational temperature model,[44,69] with the primary difference being its use of StS kinetics. The simulation conditions are chosen to encompass different degrees of thermochemical nonequilibrium behind the normal shock, corresponding to different flight altitudes and Mach numbers as detailed in Table III (Cases 3–6), and the incoming gas consists of 79% of N_2 and 21% of O_2 with the Boltzmann vibrational distributions.

A. Coarse-grained results

Figure 9 illustrates the profiles of translational and vibrational temperatures for N_2, O_2, and NO behind the normal shock wave under cases 3–6 conditions obtained by using different models. The x-coordinate time is interchangeable with the post-shock position via $t = x/U_\infty$. Immediately behind the shock, vibrational excitation occurs, followed by a significant increase in dissociation and the onset of ZE processes due to the atomic products. As the upstream Mach number increases (from 8 to 16), the post-shock temperature rises significantly. The CGM-2G results generally align well with the StS results across all cases, with slight differences noticeable for the NO vibrational temperature. When the number of vibrational groups of the molecule is increased from 2 to 3 (and beyond), an even closer alignment with the StS results can be achieved, although this is not explicitly depicted in the figure for simplicity. In contrast, the CGM-1G model fails to reproduce the StS results, significantly underestimating both translational and vibrational temperatures. This discrepancy arises because the CGM-1G model tends to overestimate N_2 and O_2 populations at higher energy levels (see the VDFs below), leading to increased dissociation rates and greater consumption of vibrational energies. As shown in Figs. 10(a) and 10(b) (for cases 4 and 6), the CGM-1G model predicts larger quantities of N and O atoms after the dissociation incubation period. Note that the variation trends for cases 4 and 6 are similar, but the relaxation processes are much slower at higher altitude. Additionally, Figs. 10(d) and 10(e) illustrate the total vibrational energy (obtained via $\sum_i n_{c,i}\varepsilon_{c,i}$) peaks for N_2 and O_2, indicating the competitive relation between vibrational excitation and dissociation. The peak of O_2 vibrational energy appears earlier than that of N_2, as O_2 dissociates more easily due to its lower dissociation energy. The total vibrational energies of N_2 and O_2 are lower for the CGM-1G model than other models due to the more considerable vibrational energy loss in dissociation (as mentioned earlier). Furthermore, for molecule NO, Fig. 9 shows that its vibrational temperature immediately behind the shock is much higher than the upstream temperature and close to post-shock translational temperature, similar to the results of cases 1 and 2. As NO molecules accumulate, the backward ZE reactions and the dissociation of NO become significant, causing the NO concentration to decrease gradually after reaching its peak. The lower NO mole fraction [Fig. 10(c)] after the peak in the CGM-1G model compared to that of other models is also due to increased dissociation caused by higher populations of high-lying NO vibrational states [see the VDF in Fig. 11(f)].

The above results demonstrate the effectiveness of reducing the original hundreds of vibrational energy states (and corresponding microscopic equations) to fewer than 6 $(2 + 2 + 2)$ vibrational groups while still achieving good agreement with the StS results in predicting the temperatures and mole fractions. However, the CGM-1G model is not accurate enough to reproduce the StS results.

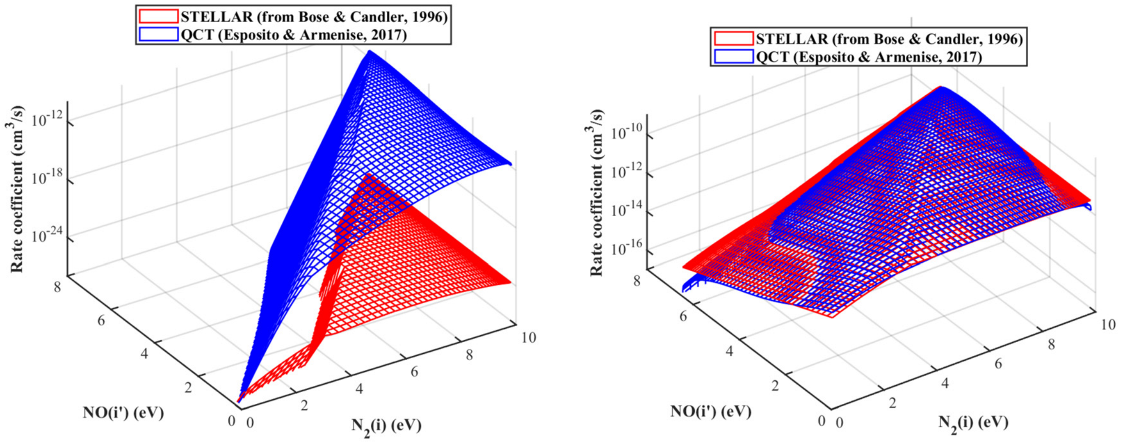

(a) $N_2(i)+O \rightarrow NO(i')+N$, T = 1000 K (b) $N_2(i)+O \rightarrow NO(i')+N$, T = 10000 K

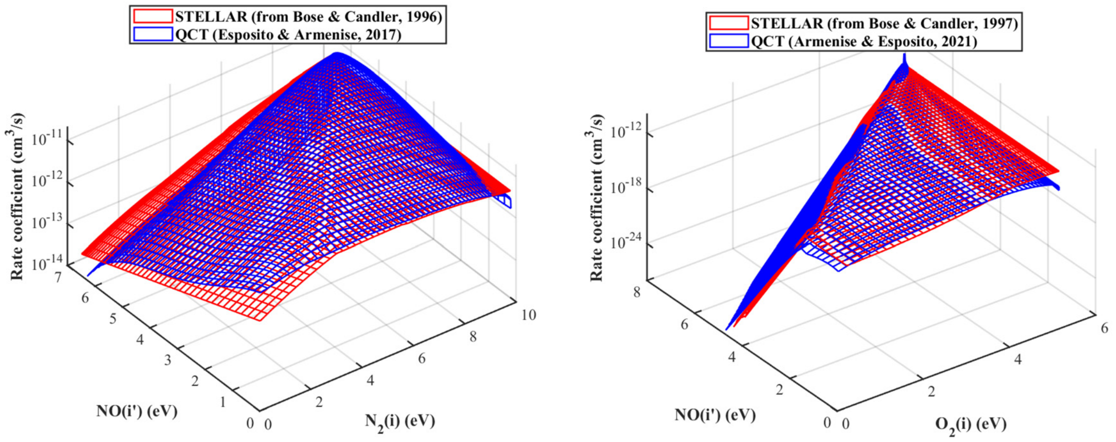

(c) $N_2(i)+O \rightarrow NO(i')+N$, T = 20000 K (d) $O_2(i)+N \rightarrow NO(i')+O$, T = 1000 K

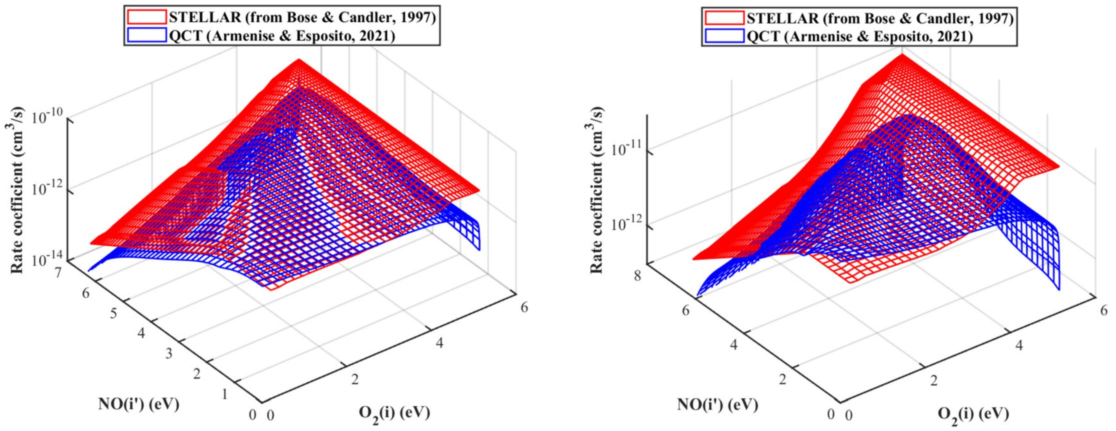

(e) $O_2(i)+N \rightarrow NO(i')+O$, T = 10000 K (f) $O_2(i)+N \rightarrow NO(i')+O$, T = 20000 K

FIG. 6. Comparison of ZE rate coefficients from the present and STELLAR database for $N_2 + O$ and $O_2 + N$ collisions.

TABLE III. Flow conditions for the StS and CGM simulations.

No.	Condition	U_∞(m/s)	T_∞(K)	p_∞ (Pa)
Case 1	77.7% N_2, 22.3% O_2	3850	300	299.98
Case 2	60% N_2, 40% O_2	3470	300	299.98
Case 3	H = 40 km, $Ma_\infty = 8$	3422.27	250.35	287.14
Case 4	H = 40 km, $Ma_\infty = 16$	6844.54	250.35	287.14
Case 5	H = 60 km, $Ma_\infty = 8$	3399.45	247.02	21.96
Case 6	H = 60 km, $Ma_\infty = 16$	6798.89	247.02	21.96

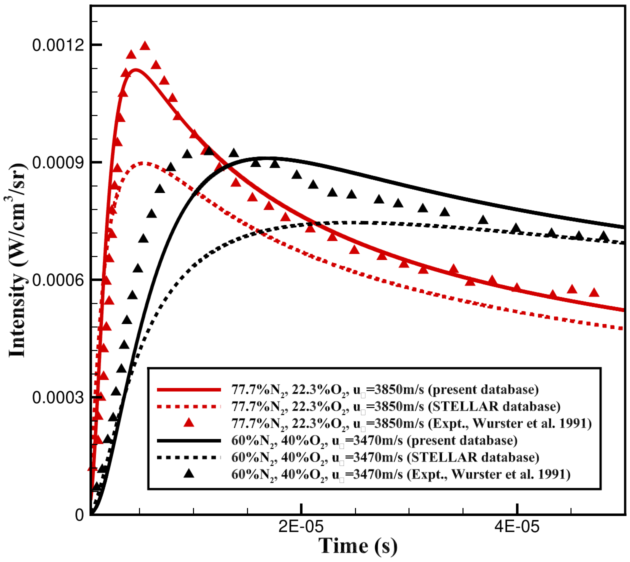

FIG. 7. Post-shock radiation intensity of the NO band obtained by the StS simulations and experiments.[66]

In the microscopic view, Figs. 11(a)–11(c) show the mole fraction variations of all vibrational energy levels of N_2, O_2, and NO, respectively, obtained by the StS model under the case 4 condition. For both N_2 and O_2, the lowest vibrational states are excited to the higher energy levels behind the shock, resulting in the overpopulation of medium and high-lying states for the StS results compared to the CGM-1G model. This effect can be seen in the VDFs at $t = 7 \times 10^{-9}$s in Figs. 11(d) and 11(e). As relaxation proceeds, the accumulation of higher vibrational energy states strengthens the dissociation rates (preferential dissociation), which in turn results in the significant depletion of high-lying states,[70] as evidenced by the almost-vertical slope in the high-energy tails of VDFs in Figs. 11(d) and 11(e). Moreover, the CGM-1G model fails to capture this important depletion of high-lying states and instead overestimates the populations of N_2 and O_2 at higher energy levels, as seen in the VDFs at $t = 5 \times 10^{-8}$s. Consequently, the dissociation rates predicted by the CGM-1G model are much higher,[35] leading to the trends observed in the temperatures (already seen in Fig. 9) and mole fractions (Fig. 10).

The VDF of NO behind the normal shock slightly differs from those of N_2 and O_2. Figure 11(f) shows that at $t = 7 \times 10^{-9}$s (note that the VDF at $t = 5 \times 10^{-8}$s is similar, so it is not shown for figure clarity), the entire vibrational ladder of NO is more excited than those of N_2 and O_2 because NO is not present in the upstream flow and is formed by the ZE reactions directly in vibrationally excited states, bypassing the need to climb the vibrational ladder.[28] As a result, the vibrational temperature of NO behind the shock is close to the translational temperature (see Fig. 9). Moreover, Fig. 11(c) shows that each NO vibrational level exhibits a peak due to the gradually increasing backward ZE reactions and the dissociation of NO. The distance of these peaks behind the shock decreases with increasing vibrational energy. The dissociation of NO also leads to significant depletion in higher energy levels, so the CGM-1G model again cannot accurately predict the high-energy tails and consequently gives stronger dissociation, leading to the total vibrational energy of NO in the CGM-1G model being lower than other models [see Fig. 10(f)].

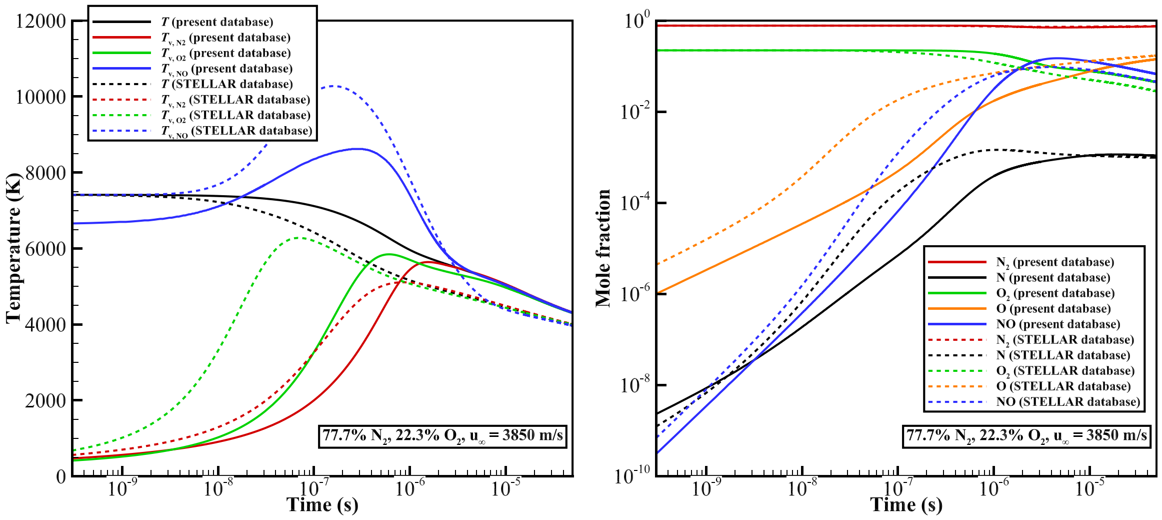

(a) Translational and vibrational temperatures (b) Mole fractions of species

FIG. 8. Simulation results for case 1 based on the present (solid lines) and STELLAR (dashed lines) databases, respectively.

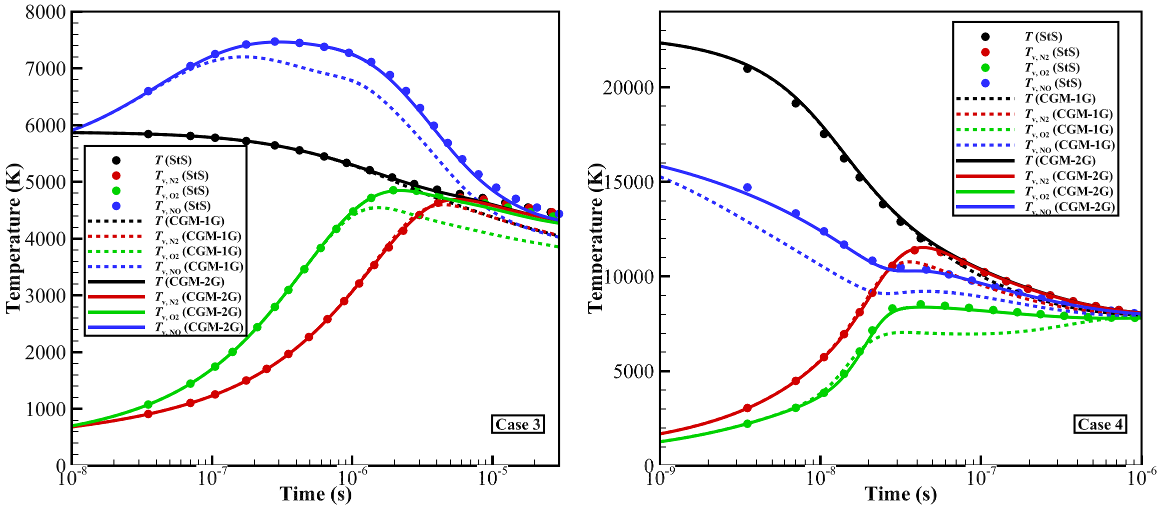

(a) Case 3: H = 40 km, Ma = 8 (b) Case 4: H = 40 km, Ma = 16

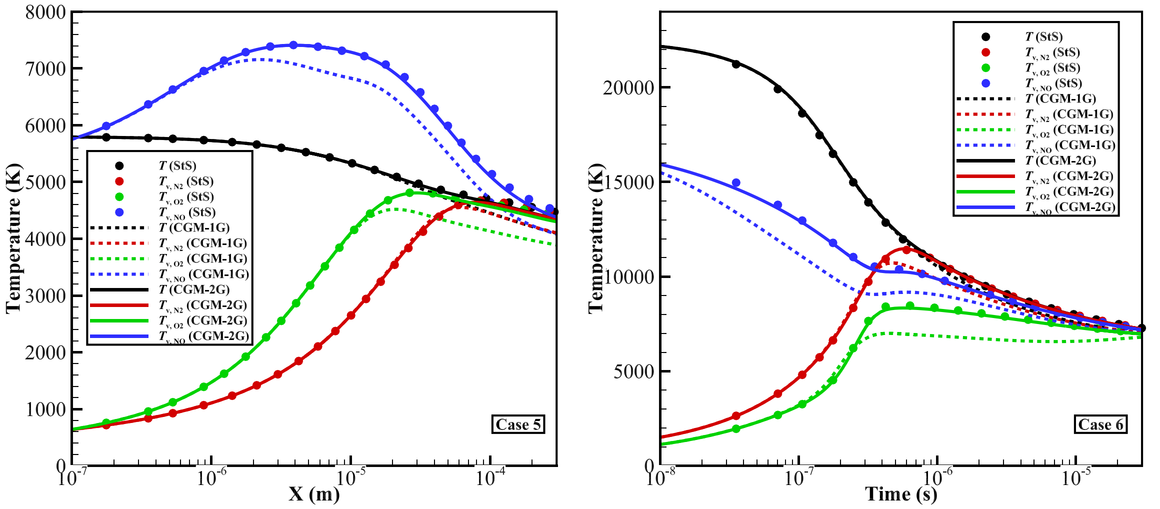

(c) Case 5: H = 60 km, Ma = 8 (d) Case 6: H = 60 km, Ma = 16

FIG. 9. Simulation results of post-shock translational and vibrational temperatures for different cases obtained by the StS (symbols), CGM-1G (dashed lines), and CGM-2G (solid lines) models, respectively.

Furthermore, Figs. 11(d)–11(f) also show the VDFs of the CGM-2G and CGM-3G models, which increasingly approach the StS results as the number of grouping increases. It is noted that the above agreement with the StS VDF can be further improved by employing high-order polynomial representations within each group.[40]

B. Energy source terms of vibrational groups for different kinetic processes

The energy source terms for vibrational groups of molecules associated with different types of kinetic processes are defined as follows:

$$\begin{aligned} W^{vib}_{c,G_i} &= \sum_{v\in G_i} \omega^{vib}_{c,v} \cdot \varepsilon_{c,v}, \\ W^{DR}_{c,G_i} &= \sum_{v\in G_i} \omega^{DR}_{c,v} \cdot \varepsilon_{c,v}, \\ W^{ZE}_{c,G_i} &= \sum_{v\in G_i} \omega^{ZE}_{c,v} \cdot \varepsilon_{c,v}, \end{aligned} \tag{26}$$

where $\omega^{vib}_{c,v}$, $\omega^{DR}_{c,v}$, and $\omega^{ZE}_{c,v}$ are defined in Eq. (8), representing the mass production rates of the vibrational inelastic (VT + VVT), DR, and ZE processes, respectively. The summation of W^{vib}_{c,G_i}, W^{DR}_{c,G_i}, and W^{ZE}_{c,G_i} gives the total energy source term of the vibrational group, namely, W^{Total}_{c,G_i}. Note that a positive *vib* energy source term indicates energy

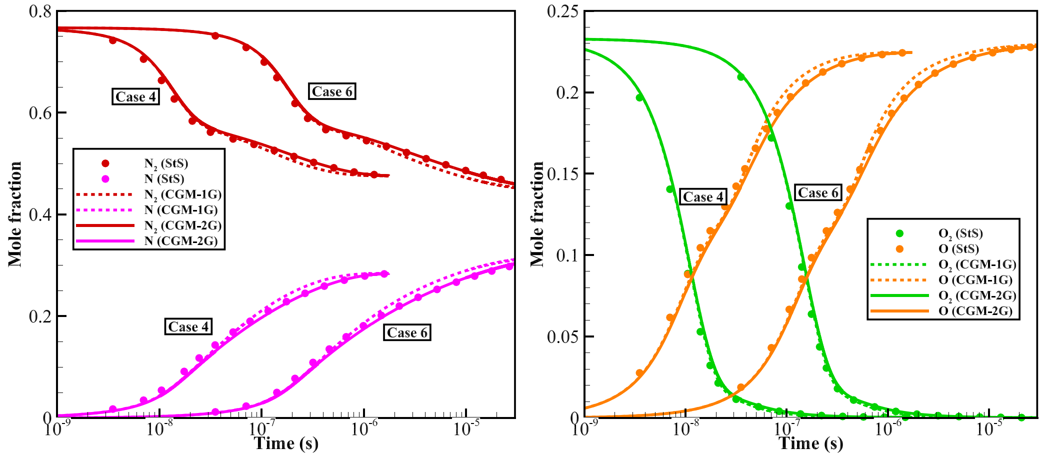

(a) Mole fractions of N_2 and N

(b) Mole fractions of O_2 and O

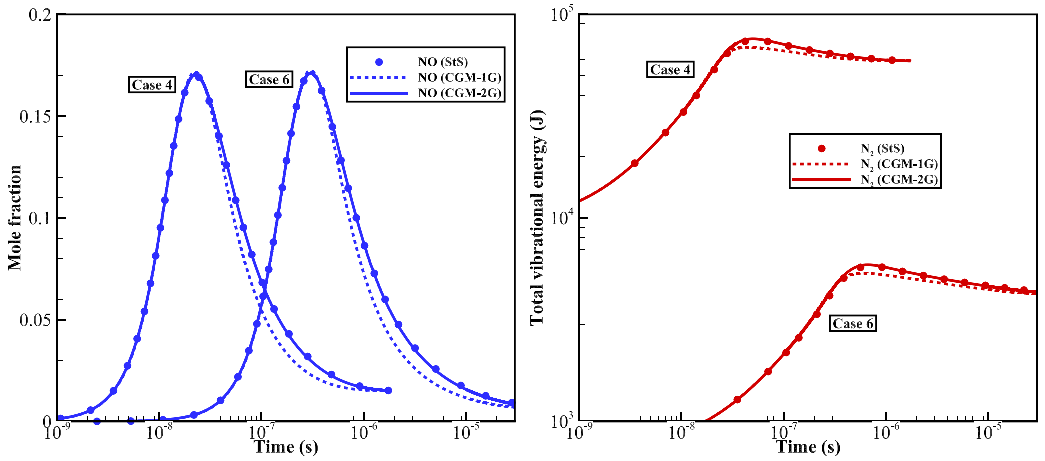

(c) Mole fraction of NO

(d) Total vibrational energy of N_2

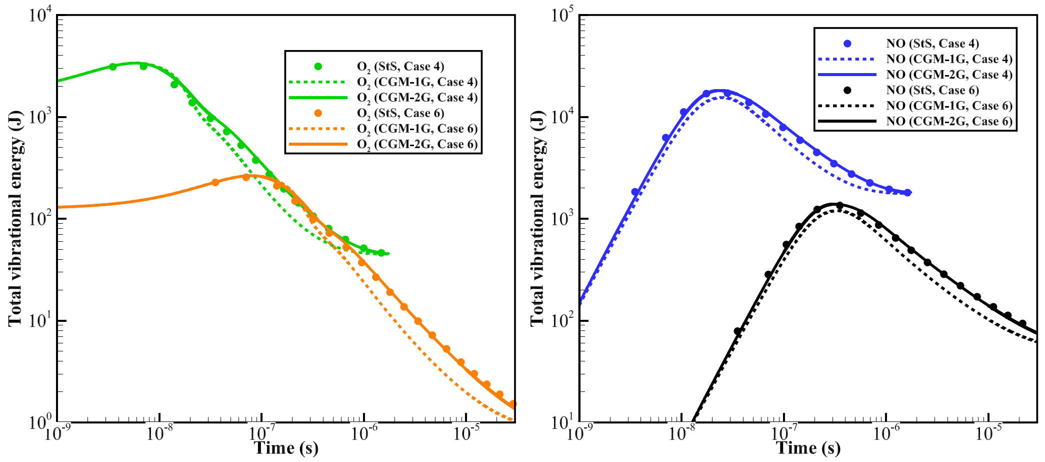

(e) Total vibrational energy of O_2

(f) Total vibrational energy of NO

FIG. 10. Mole fractions of species and total vibrational energies of diatoms behind the normal shock for cases 4 and 6.

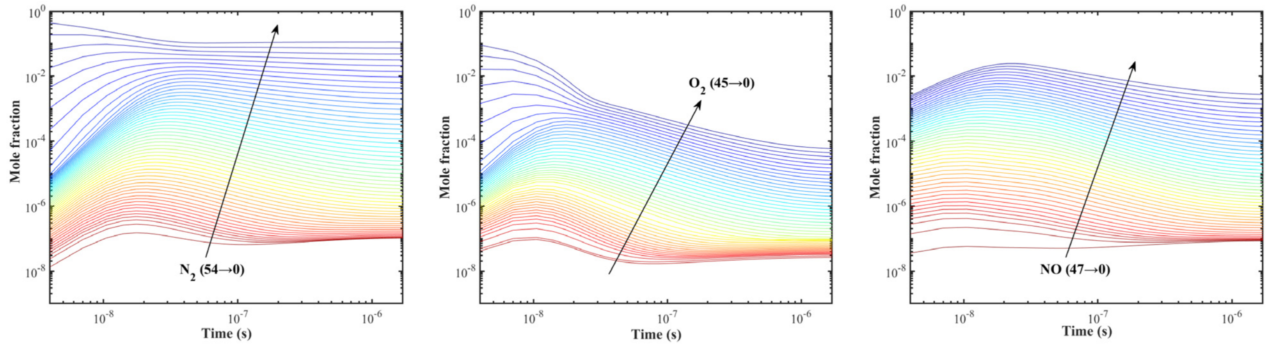

(a) Mole fractions of N_2 vibrational states (b) Mole fractions of O_2 vibrational states (c) Mole fractions of NO vibrational states

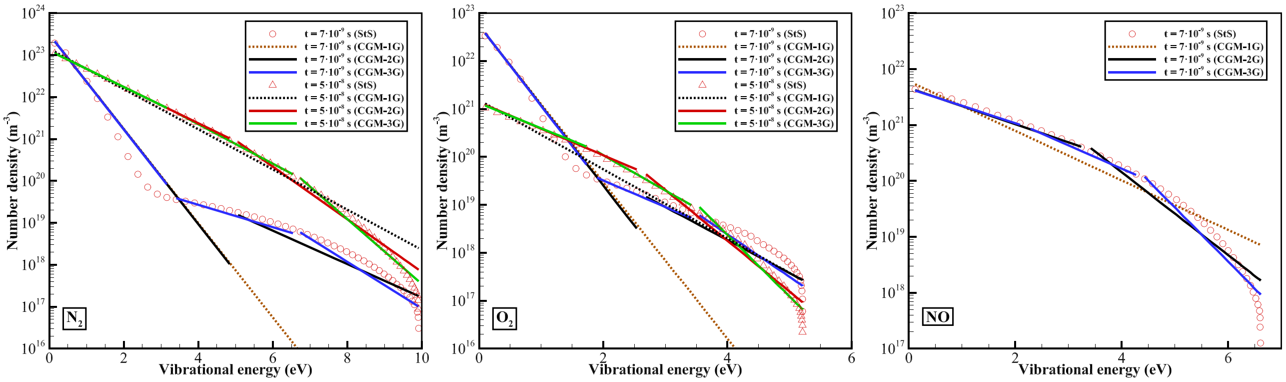

(d) VDFs of N_2 (e) VDFs of O_2 (f) VDFs of NO

FIG. 11. Mole fractions (obtained by the StS model) and VDFs of N_2, O_2, and NO (obtained by different models) under case 4 condition.

transferring into the vibrational group by inelastic collision, while positive DR and ZE terms indicate that the molecule is generated and populated in the vibrational group.

The low-, medium-, and high-lying vibrational states are generally controlled mainly by distinct physical mechanisms.[71] In a previous study for the O_2/O binary gas system,[35] O_2 at lower vibrational levels are found to relax mainly through inelastic collisions, while those at the highest levels are significantly influenced by dissociation. The medium-lying energy levels act as a bridge for energy transfer between the above two vibrational groups. Therefore, in the following, we discuss the energy source terms of vibrational groups under the 3 G assumption by categorizing molecules into G_1, G_2, and G_3 groups based on energy criterion (see Table IV) to investigate their distinct behaviors during the post-shock relaxation.

The energy source terms defined in Eq. (26) for G_1, G_2, and G_3 groups of N_2, O_2, and NO, respectively, are depicted in Figs. 12–14 for the case 4 condition. Specifically, Fig. 12(a) shows that the group G_1 of N_2 is mainly governed by inelastic vibrational excitation processes, which feed the energy from translational energy, and the dissociation has little influence on this group. The ZE energy source term initially becomes negative due to the forward ZE process 21 (see Table I), in which the reactants are manly states in the group G_1, and subsequently turns positive due to the enhancement of the backward ZE process 21. Figure 12(b) shows the fraction of group G_1 in N_2, illustrating that the states are either excited to higher levels or consumed by the forward ZE process 21 so that the fraction of group G_1 first decreases. A local minimum is observed due to the increased dissociation that consumes groups G_2 and G_3 (see below), subsequently reinforcing the dominance of group G_2. As seen in Figs. 12(c) and 12(e), groups G_2 and G_3 of N_2 are notably influenced by dissociation, which is negative in the energy source term. In contrast, both the ZE and inelastic processes contribute as sources for groups G_2 and G_3, which explains the initial increase in their fractions up to approximately $t = 3 \times 10^{-8}$ s [see Figs. 12(d) and 12(f)].

TABLE IV. Energy levels within each group in 3 G assumption.

	N_2	O_2	NO
G_1	0–11	0–9	0–9
G_2	12–26	10–20	10–21
G_3	27–54	21–45	22–47

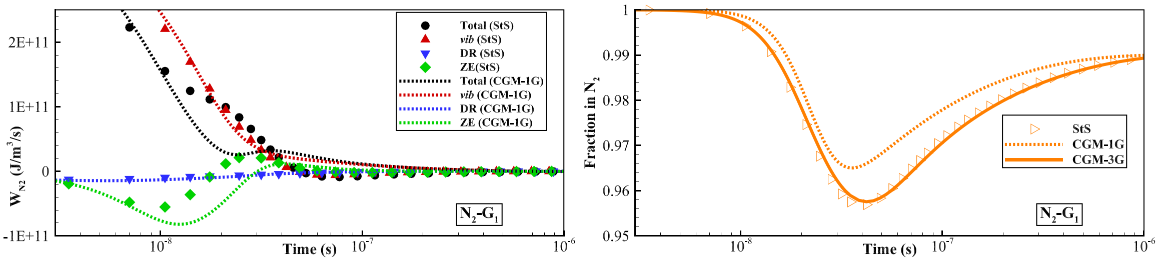

(a) Energy source terms of Group 1 of N_2 (b) Mole fractions of Group 1 of N_2

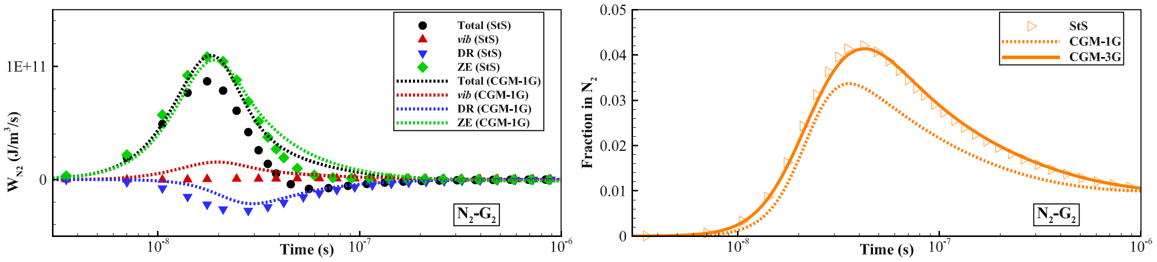

(c) Energy source terms of Group 2 of N_2 (d) Mole fractions of Group 2 of N_2

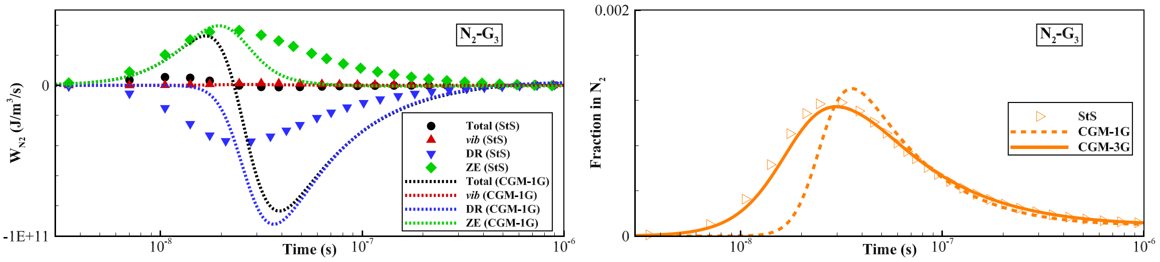

(e) Energy source terms of Group 3 of N_2 (f) Mole fractions of Group 3 of N_2

FIG. 12. Energy source terms and fractions of different vibrational groups of N_2 obtained by the StS (symbols) and CGM (lines) models.

Note that the positive ZE energy source term, which is even larger than the *vib* contribution, arises from the fact that the backward ZE process 21 produces N_2 with higher vibrational energy. Local maxima are observed for the fractions of groups G_2 and G_3 in N_2, corresponding to the regions where the DR energy source terms reach their peak values.

Moreover, as shown in Fig. 13, the behavior of O_2 differs from that of N_2 due to its easier and more pronounced dissociation. For group G_1 in O_2, the DR energy source term is significant, meaning the dissociation from the lower vibrational state is pronounced due to the high post-shock temperature. Therefore, the total energy source term is not always positive for group G_1, despite the presence of significant vibrational excitation. The ZE energy source term for O_2 exhibits similarities to that of N_2: the forward ZE process 22 (see Table I) initially depletes the group G_1, followed by a subsequent positive energy source term attributed to the enhanced backward ZE process 22. Additionally, the backward reaction of ZE process 22 is more effective than the forward reaction for groups G_2 and G_3, accounting mostly for their initial rise in fractions up to approximately $t = 3 \times 10^{-8}$ s [see Figs. 13(d) and 13(f)]. Therefore, the presence of ZE reactions indirectly facilitates the energy transfer in N_2 and O_2, which does not occur in the binary O_2/O or N_2/N gas systems. Local maxima are also observed for the fractions of groups G_2 and G_3 in O_2, while in the region far behind the shock, the fraction of G_3 increases due to the competition between ZE and dissociation processes.

Figure 14 shows the energy source terms of vibrational groups of NO. As depicted in Figs. 14(g) and 14(h) about the total energy source term and number density of NO, the post-shock NO molecules are initially generated from the forward ZE reactions, and as NO accumulates in the system, its dissociation process and backward ZE reactions gradually become dominant, leading to the substantial consumption of NO. The group G_1 of NO is primarily governed by the ZE reaction, as indicated in Fig. 14(a) where the curves of total and ZE energy source terms are close. Moreover, it is noteworthy that the post-shock fractions of groups G_2 and G_3 in NO are significantly higher compared to those in N_2 and O_2, meaning that forward ZE reactions efficiently

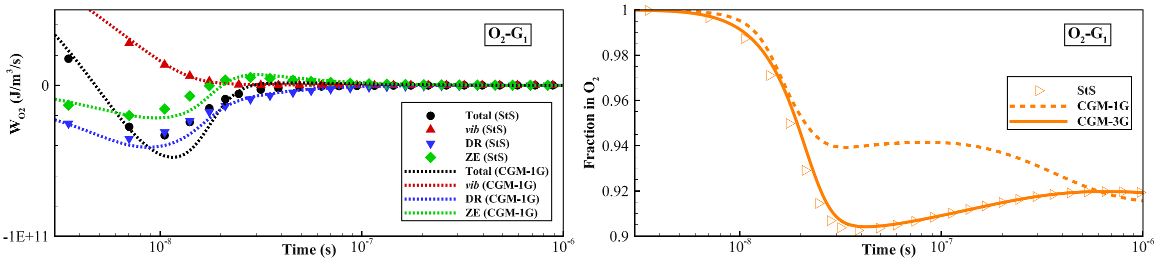

(a) Energy source terms of Group 1 of O_2 (b) Mole fractions of Group 1 of O_2

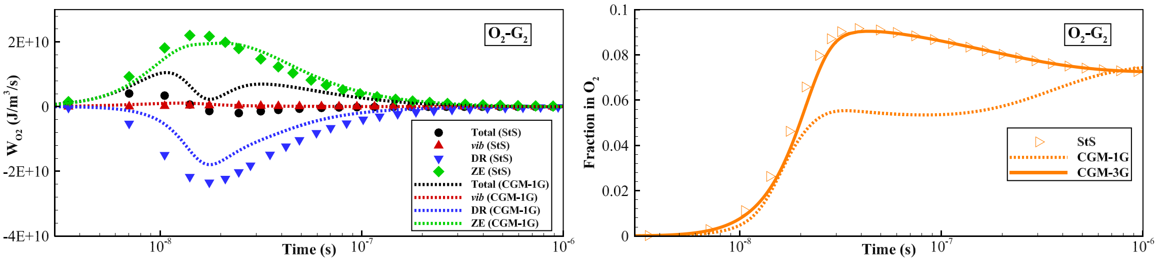

(c) Energy source terms of Group 2 of O_2 (d) Mole fractions of Group 2 of O_2

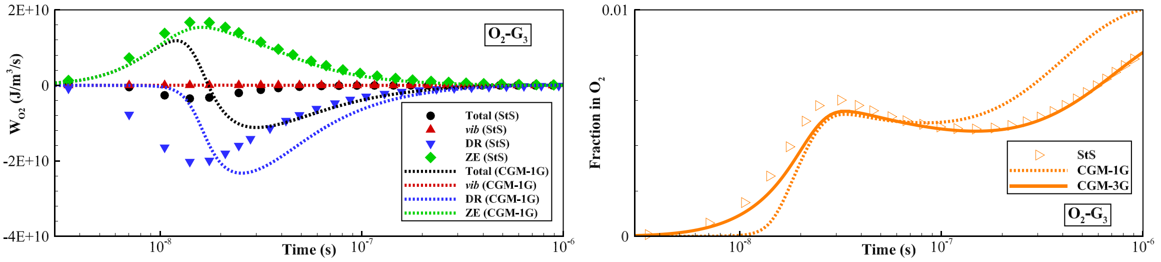

(e) Energy source terms of Group 3 of O_2 (f) Mole fractions of Group 3 of O_2

FIG. 13. Energy source terms and fractions of different vibrational groups of O_2 obtained by the StS (symbols) and CGM (lines) models.

produce NO at higher vibrational energies, resulting in a higher vibrational temperature of NO (see Fig. 9). These two fractions [see Figs. 14(d) and 14(f)] decrease monotonically behind the shock since the significant dissociation and the post-shock vibrational temperature of NO is higher than the equilibrium temperature far from the shock. Furthermore, the contribution of inelastic processes to the energy source term is minimal for groups G_2 and G_3 in NO.

Figures 12–14 also compare the results of the StS and CGMs. For the group G_1 of N_2 and O_2, the CGM-1G results match the StS results for the inelastic energy source term and the vibrational temperatures are close initially [see Fig. 9(b)], indicating that the excitation of the lower vibrational states follows the Landau–Teller behavior. However, significant discrepancies emerge as relaxation progresses and dissociation becomes dominant. As seen from the VDFs in Figs. 11(d) and 11(e), the CGM-1G model initially underestimates the number density of higher vibrational states compared to the StS results, particularly in group G_3. Consequently, significant dissociation starts later in the CGM-1G model, causing the DR energy source terms to rise later for groups G_2 and G_3 of N_2 and O_2 and the atomic N and O are produced slowly. Furthermore, as dissociation becomes significant, group G_3 of N_2 and O_2 predicted by the CGM-1G model exhibits overpopulation characteristics [see Figs. 11(d) and 11(e)]. This occurs because the CGM-1G model does not accurately represent the substantial depletion of very high energy levels resulting from preferential dissociation, causing the number density of group G_3 to remain higher. Consequently, the overestimation of group G_3 in the CGM-1G model leads to significantly higher dissociation rates for O_2 and N_2, which then generate more atomic N and O [as seen in Figs. 10(a) and 10(b)] and cause much greater vibrational energy removal during dissociation, reflected in the higher DR energy source terms for the G_3 group of N_2 and O_2. The higher substantial vibrational energy loss results in a significantly lower $T_{v,c}$ (and also T) in the CGM-1G model, as shown in Fig. 9(b). The above behavior of initial underpopulation followed by overpopulation of high-lying vibrational states in the CGM-1G model is evident in the fractions of group G_3 of N_2 and O_2 in Figs. 12(f) and 13(f), respectively.

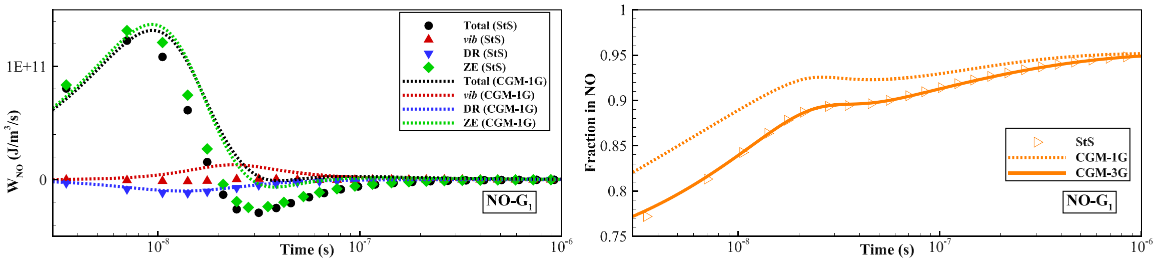

(a) Energy source terms of Group 1 of NO

(b) Mole fractions of Group 1 of NO

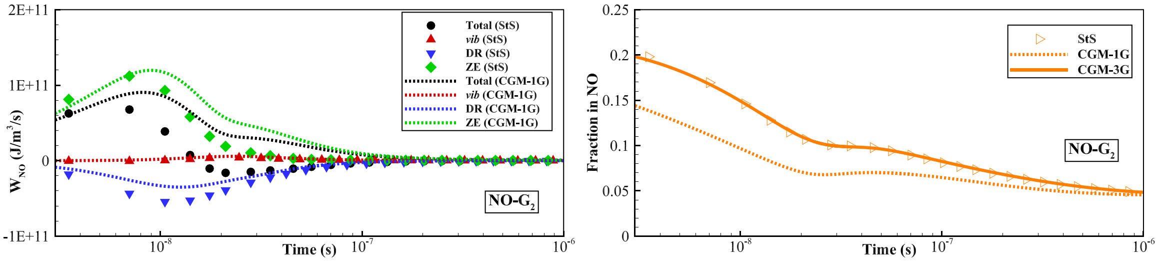

(c) Energy source terms of Group 2 of NO

(d) Mole fractions of Group 2 of NO

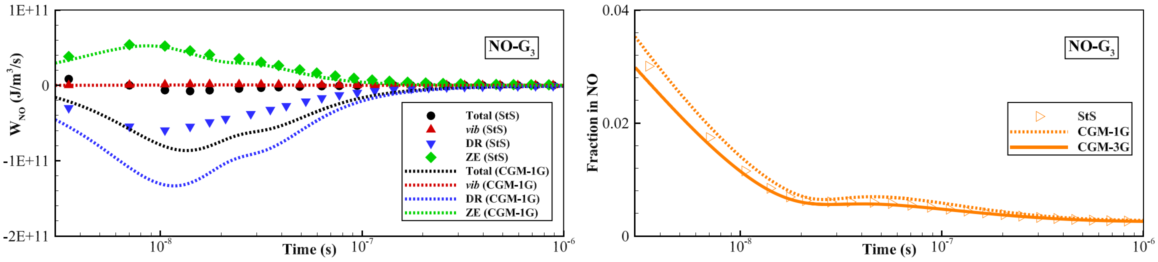

(e) Energy source terms of Group 3 of NO

(f) Mole fractions of Group 3 of NO

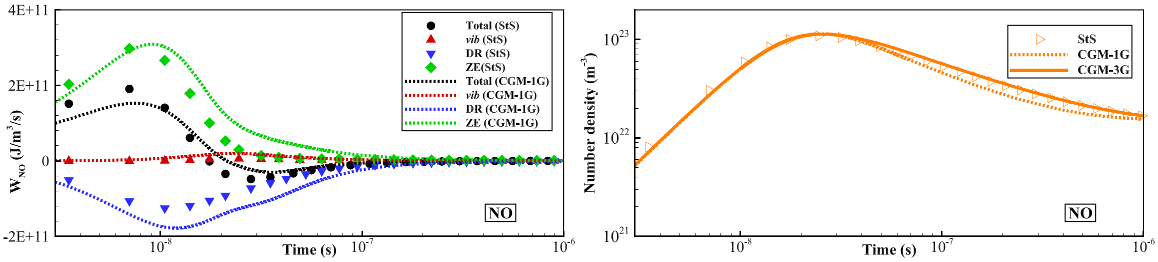

(g) Energy source terms of NO

(h) Number densities of NO

FIG. 14. Energy source terms and fractions of different vibrational groups of NO obtained by the StS (symbols) and CGM (lines) models. Energy source terms and number densities of NO are also shown.

For NO, the differences between the CGM-1G and StS models shown in the curves of VDFs in Fig. 11(f) are consistent with the fractions given in Fig. 14: The CGM-1G model overestimates the fractions of groups G_1 and G_3, while underestimating group G_2, due to its simplified representation of VDF with a straight-line. The overestimation of group G_3 in NO leads to higher dissociation rates in the CGM-1G model, resulting in greater NO depletion compared to the StS model, similar to the cases in N_2 and O_2.

The above results indicate that the CGM-1G model, belonging to the multi-vibrational temperature model but employing the updated StS kinetics, fails to reproduce the StS results due to its difficulty in accurately predicting the VDF, especially for higher vibrational states. The overestimation of number densities in high-lying vibrational states in the CGM-1G model leads to higher dissociation rates of molecules and increased consumption of their vibrational energy during dissociation. The aforementioned non-Boltzmann effects provide insights into developing the multi-temperature reduced-order model for air species that achieves accuracy comparable to the StS model while maintaining computational efficiency for practical applications.

V. CONCLUSIONS

We developed a comprehensive vibrational state-specific rate coefficient database (Table I) within the temperature range of 300–25 000 K for simulating high-enthalpy thermochemical nonequilibrium air flows. This database incorporates recent QCT molecular dynamics simulations from the literature for $N_2 + N_2$, $N_2 + N$, $N_2 + O$, and $O_2 + N$ collisions, and the theoretical FHO model for inelastic collisions and MT model for dissociation are employed to complement the rate coefficients unavailable from molecular dynamics calculations. The post-shock StS simulations using the present database showed better agreement with the shock-tube experimental data of the infrared radiation of NO molecules than those using the STELLAR database.

Based on the updated kinetic database, we studied the post-shock high-enthalpy thermochemical nonequilibrium flows of five-species air mixtures using the StS and CGMs under different freestream conditions. The results indicate that the CGMs with two (CGM-2G) or more groups for each molecule (N_2, O_2, and NO) provide translational and vibrational temperatures, mass fractions, and vibration energy of molecules that are close to the StS results. Although the VDF is not fully reproduced, these CGMs still perform well in predicting macroscopic quantities. However, the CGM-1G model, which employs only one group per molecule and thus falls under the multi-vibrational temperature framework (but uses StS kinetics), fails to reproduce the StS results accurately. The inaccuracy of the CGM-1G model stems from its inaccurate prediction of the VDF, which exhibits a significant overpopulation of the high vibrational energy tails for N_2 and O_2 during the dissociation-dominated stage. This overpopulation leads to an increased rate of dissociation and excessive consumption of vibrational energy compared to the StS results. Further analysis of the vibrational energy source terms for different types of kinetic processes and fractions of vibrational groups confirmed that the deficiency of the CGM-1G model arises from the overestimation of number densities in high-lying vibrational energy levels. Moreover, the analysis of vibrational energy source terms also indicates that the presence of ZE reactions indirectly facilitates energy transfer in N_2 and O_2, which is a phenomenon not observed in binary O_2/O or N_2/N gas systems. The present findings have important implications for developing multi-vibrational temperature reduced-order models for air mixtures based on coarse-grained treatment.

ACKNOWLEDGMENTS

Q. Hong was supported by the Strategic Priority Research Program of the Chinese Academy of Sciences (Grant No. XDB0620201), the fellowship of the China Postdoctoral Science Foundation (Grant No. 2022M723233), and the National Natural Science Foundation of China (Grant No. 12302391). The authors would like to thank Dr. Fabrizio Esposito for sharing the Fortran subroutines for the fitting formulas of the StS rate coefficients of $N_2 + O$ collisions.

AUTHOR DECLARATIONS

Conflict of Interest

The authors have no conflicts to disclose.

Author Contributions

Yifeng Huang: Data curation (equal); Formal analysis (equal); Investigation (equal); Validation (equal); Visualization (equal); Writing – original draft (equal); Writing – review & editing (equal). **Qizhen Hong:** Conceptualization (equal); Data curation (equal); Formal analysis (equal); Funding acquisition (equal); Investigation (equal); Methodology (equal); Supervision (equal); Validation (equal); Writing – original draft (equal); Writing – review & editing (equal). **Sangdi Gu:** Formal analysis (equal); Investigation (equal); Writing – original draft (equal); Writing – review & editing (equal). **Xiaoyong Wang:** Formal analysis (equal); Investigation (equal); Visualization (equal); Writing – review & editing (equal). **Quanhua Sun:** Conceptualization (equal); Project administration (equal); Resources (equal); Supervision (equal); Writing – original draft (equal); Writing – review & editing (equal).

DATA AVAILABILITY

The data that support the findings of this study are available within the article.

APPENDIX: VIBRATIONAL LADDERS OF N_2, O_2, AND NO

The vibrational energy values (for which the zero-energy is fixed at the bottom of the potential well) of the molecules used in this paper are shown in Table V. The vibrational ladders of O_2 and NO molecules are taken from the STELLAR database[19] and determined through the reconstruction of the ground-state potential curve according to the Rydberg–Klein–Rees method, which

TABLE V. Vibrational ladders of N_2, O_2, and NO. Units of energies are eV.

v	ε_{v,N_2}	ε_{v,O_2}	$\varepsilon_{v,NO}$
0	0.146 99	0.097 62	0.117 62
1	0.438 38	0.290 59	0.350 21
2	0.726 31	0.480 63	0.579 31
3	1.010 72	0.667 77	0.804 94
4	1.291 60	0.852 04	1.027 10
5	1.568 89	1.033 48	1.245 79
6	1.842 59	1.212 07	1.461 02
7	2.112 66	1.387 86	1.672 79
8	2.379 10	1.560 82	1.881 09
9	2.641 88	1.730 92	2.085 93
10	2.901 00	1.898 30	2.287 30
11	3.156 46	2.062 82	2.485 20

TABLE V. (*Continued.*)

ν	ε_{ν,N_2}	ε_{ν,O_2}	$\varepsilon_{\nu,NO}$
12	3.408 25	2.224 49	2.679 62
13	3.656 35	2.383 44	2.870 55
14	3.900 78	2.539 53	3.057 97
15	4.141 53	2.692 65	3.241 86
16	4.378 58	2.843 04	3.422 22
17	4.611 93	2.990 46	3.599 02
18	4.841 58	3.134 90	3.772 24
19	5.067 50	3.276 36	3.941 84
20	5.289 67	3.415 97	4.107 81
21	5.508 08	3.550 73	4.270 10
22	5.722 70	3.682 03	4.428 69
23	5.933 49	3.809 36	4.583 54
24	6.140 41	3.932 72	4.734 60
25	6.343 41	4.052 00	4.882 33
26	6.542 44	4.166 93	5.025 45
27	6.737 44	4.277 40	5.164 31
28	6.928 34	4.383 03	5.298 66
29	7.115 05	4.483 83	5.428 32
30	7.297 50	4.579 54	5.553 17
31	7.475 59	4.669 93	5.672 95
32	7.649 21	4.754 60	5.787 44
33	7.818 24	4.833 33	5.896 40
34	7.982 55	4.905 99	5.999 55
35	8.142 01	4.971 82	6.096 58
36	8.296 46	5.030 71	6.187 14
37	8.445 73	5.081 92	6.270 80
38	8.589 64	5.124 69	6.347 08
39	8.727 99	5.158 04	6.415 35
40	8.860 57	5.180 98	6.474 82
41	8.987 12	5.193 87	6.524 37
42	9.107 40	5.201 56	6.562 37
43	9.221 12	5.207 26	6.586 13
44	9.327 94	5.211 23	6.596 26
45	9.427 54	5.213 09	6.603 06
46	9.519 51		6.608 49
47	9.603 43		6.612 23
48	9.678 83		
49	9.745 14		
50	9.801 78		
51	9.848 05		
52	9.883 20		
53	9.906 38		
54	9.916 78		

improves the determination of the higher vibrational levels close to the dissociation limit. Moreover, the vibrational ladder of N_2 is adopted from Fangman and Andrienko[48] based on the diatomic potential energy curve of N_2 in the Minnesota N_4 ground PES.[49]

REFERENCES

[1] G. V. Candler, "Rate effects in hypersonic flows," Annu. Rev. Fluid Mech. **51**, 379–402 (2019).

[2] P. A. Gnoffo, K. J. Weilmuenster, R. D. Braun, and C. I. Cruz, "Influence of sonic-line location on Mars pathfinder probe aerothermodynamics," J. Spacecr. Rockets **33**, 169–177 (1996).

[3] C. Park, *Nonequilibrium Hypersonic Aerothermodynamics* (Wiley, 1990).

[4] C. Park, "Assessment of two-temperature kinetic model for ionizing air," J. Thermophys. Heat Transfer **3**, 233–244 (1989).

[5] L. Landau, "Theory of sound dispersion," Phys. Z. Sowjetunion **10**, 34–43 (1936).

[6] P. V. Marrone and C. E. Treanor, "Chemical relaxation with preferential dissociation from excited vibrational levels," Phys. Fluids **6**, 1215–1221 (1963).

[7] S. Macheret, A. Fridman, I. Adamovich, J. Rich, and C. Treanor, "Mechanisms of nonequilibrium dissociation of diatomic molecules," in *AIAA/ASME 6th Joint Thermophysics and Heat Transfer Conference, 1994* (AIAA, 1994), p. 94.

[8] R. S. Chaudhry, I. D. Boyd, E. Torres, T. E. Schwartzentruber, and G. V. Candler, "Implementation of a chemical kinetics model for hypersonic flows in air for high-performance CFD," in *AIAA Scitech 2020 Forum* (AIAA, 2020), p. 2191.

[9] X. Wang, Q. Hong, Y. Hu, and Q. Sun, "On the accuracy of two-temperature models for hypersonic nonequilibrium flow," Acta Mech. Sin. **39**, 122193 (2023).

[10] C. Park, "The limits of two-temperature kinetic model in air," AIAA Paper No. 2010-911, 2010.

[11] E. Nagnibeda and E. Kustova, *Non-Equilibrium Reacting Gas Flows: Kinetic Theory of Transport and Relaxation Processes* (Springer Science & Business Media, 2009).

[12] Q. Hong, X. Wang, Y. Hu, and Q. Sun, "Development of a stagnation streamline model for thermochemical nonequilibrium flow," Phys. Fluids **32**, 046102 (2020).

[13] S. Gu, J. Hao, and C.-Y. Wen, "State-specific study of air in the expansion tunnel nozzle and test section," AIAA J. **60**, 4024–4038 (2022).

[14] W. Su, D. Bruno, and Y. Babou, "State-specific modeling of vibrational relaxation and nitric oxide formation in shock-heated air," J. Thermophys. Heat Transfer **32**, 337–352 (2018).

[15] F. Esposito, I. Armenise, G. Capitta, and M. Capitelli, "O-O_2 state-to-state vibrational relaxation and dissociation rates based on quasiclassical calculations," Chem. Phys. **351**, 91–98 (2008).

[16] F. Esposito, I. Armenise, and M. Capitelli, "N-N_2 state to state vibrational-relaxation and dissociation rates based on quasiclassical calculations," Chem. Phys. **331**, 1–8 (2006).

[17] D. Bose and G. V. Candler, "Thermal rate constants of the N_2+O →NO+N reaction using *ab initio* $^3A''$ and $^3A'$ potential energy surfaces," J. Chem. Phys. **104**, 2825–2833 (1996).

[18] D. Bose and G. V. Candler, "Thermal rate constants of the O_2+N →NO+O reaction based on the $^2A'$ and $^4A'$ potential-energy surfaces," J. Chem. Phys. **107**, 6136–6145 (1997).

[19] M. L. Da Silva, B. Lopez, V. Guerra, and J. Loureiro, "A multiquantum state-to-state model for the fundamental states of air and application to the modeling of high-speed shocked flows," in 5th International Workshop Radiation of High Temperature Gases in Atmospheric Entry, ESA SP, Vol. 714 (2012).

[20] S. Gu, J. Hao, and C.-Y. Wen, "On the vibrational state-specific modeling of radiating normal shocks in air," AIAA J. **60**, 3760–3774 (2022).

[21] Q. Hong, Q. Sun, F. Pirani, M. A. Valentín-Rodríguez, R. Hernández-Lamoneda, C. Coletti, M. I. Hernández, and M. Bartolomei, "Energy exchange rate coefficients from vibrational inelastic O_2 ($\sum$ g-3) + O_2 ($\sum$ g-3) collisions on a new spin-averaged potential energy surface," J. Chem. Phys. **154**, 064304 (2021).

[22] Q. Hong, L. Storchi, Q. Sun, M. Bartolomei, F. Pirani, and C. Coletti, "Improved quantum–classical treatment of $N_2 - N_2$ inelastic collisions: Effect of the potentials and complete rate coefficient data sets," J. Chem. Theory Comput. **19**, 8557–8571 (2023).

[23] F. Esposito and I. Armenise, "Reactive, inelastic, and dissociation processes in collisions of atomic oxygen with molecular nitrogen," J. Phys. Chem. A **121**, 6211–6219 (2017).

[24] I. Armenise and F. Esposito, "$N + O_2(v)$ collisions: Reactive, inelastic and dissociation rates for state-to-state vibrational kinetic models," Chem. Phys. **551**, 111325 (2021).

[25] O. Kunova and E. Nagnibeda, "State-to-state description of reacting air flows behind shock waves," Chem. Phys. **441**, 66–76 (2014).

[26] L. Campoli, O. Kunova, E. Kustova, and M. Melnik, "Models validation and code profiling in state-to-state simulations of shock heated air flows," Acta Astronaut. **175**, 493–509 (2020).

[27] F. Bonelli, M. Tuttafesta, G. Colonna, L. Cutrone, and G. Pascazio, "An MPI-CUDA approach for hypersonic flows with detailed state-to-state air kinetics using a GPU cluster," Comput. Phys. Commun. **219**, 178–195 (2017).

[28] B. Lopez and M. Lino Da Silva, "Non-Boltzmann analysis of hypersonic air re-entry flows," AIAA Paper No. 2014-2547, 2014.

[29] S. F. Gimelshein, I. J. Wysong, A. J. Fangman, D. A. Andrienko, O. V. Kunova, E. V. Kustova, F. Morgado, C. Garbacz, M. Fossati, and K. M. Hanquist, "Kinetic and continuum modeling of high-temperature air relaxation," J. Thermophys. Heat Transfer **36**, 870–893 (2022).

[30] E. Torres, E. C. Geistfeld, and T. E. Schwartzentruber, "High-temperature nonequilibrium air chemistry from first principles," J. Thermophys. Heat Transfer **38**, 1–32 (2023).

[31] X. Wang, J. Guo, Q. Hong, and S. Li, "High-fidelity state-to-state modeling of hypersonic flow over a double cone," Phys. Fluids **35**, 116101 (2023).

[32] A. Guy, A. Bourdon, and M. Y. Perrin, "Consistent multi-internal-temperatures models for nonequilibrium nozzle flows," Chem. Phys. **420**, 15–24 (2013).

[33] Y. Liu, M. Panesi, A. Sahai, and M. Vinokur, "General multi-group macroscopic modeling for thermo-chemical non-equilibrium gas mixtures," J. Chem. Phys. **142**, 134109 (2015).

[34] J. Hao and C.-Y. Wen, "Maximum entropy modeling of oxygen vibrational excitation and dissociation," Phys. Rev. Fluids **4**, 053401 (2019).

[35] J. Lv, Q. Hong, X. Wang, Y. Huang, and Q. Sun, "A two-temperature thermochemical nonequilibrium model based on the coarse-grained treatment of molecular vibrational states," Phys. Rev. E **110**, 035107 (2024).

[36] Y. Liu, M. Vinokur, M. Panesi, and T. Magin, "A multi-group maximum entropy model for thermo-chemical non-equilibrium," AIAA Paper No. 2010-4332, 2010.

[37] T. E. Magin, M. Panesi, A. Bourdon, R. L. Jaffe, and D. W. Schwenke, "Coarse-grain model for internal energy excitation and dissociation of molecular nitrogen," Chem. Phys. **398**, 90–95 (2012).

[38] R. L. Macdonald, R. L. Jaffe, D. W. Schwenke, and M. Panesi, "Construction of a coarse-grain quasi-classical trajectory method. I. Theory and application to N2-N2 system," J. Chem. Phys. **148**, 054309 (2018).

[39] I. Zanardi, S. Venturi, and M. Panesi, "Adaptive physics-informed neural operator for coarse-grained non-equilibrium flows," Sci. Rep. **13**, 15497 (2023).

[40] M. P. Sharma, Y. Liu, and M. Panesi, "Coarse-grained modeling of thermochemical nonequilibrium using the multigroup maximum entropy quadratic formulation," Phys. Rev. E **101**, 013307 (2020).

[41] G. Colonna, L. D. Pietanza, and M. Capitelli, "Recombination-assisted nitrogen dissociation rates under nonequilibrium conditions," J. Thermophys. Heat Transfer **22**, 399–406 (2008).

[42] E. Kustova, E. Nagnibeda, T. Y. Alexandrova, and A. Chikhaoui, "Non-equilibrium dissociation rates in expanding flows," Chem. Phys. Lett. **377**, 663–671 (2003).

[43] J. Lv, Q. Hong, X. Wang, Z. Mao, and Q. Sun, "Deepstsnet: Reconstructing the quantum state-resolved thermochemical nonequilibrium flowfield using deep neural operator learning with scarce data," J. Comput. Phys. **491**, 112344 (2023).

[44] G. V. Candler and R. W. MacCormack, "Computation of weakly ionized hypersonic flows in thermochemical nonequilibrium," J. Thermophys. Heat Transfer **5**, 266–273 (1991).

[45] C. Jacobsen, I. Zanardi, S. Bhola, K. Duraisamy, and M. Panesi, "Information theoretic clustering for coarse-grained modeling of non-equilibrium gas dynamics," J. Comput. Phys. **507**, 112977 (2024).

[46] R. D. Levine and R. B. Bernstein, *Molecular Reaction Dynamics and Chemical Reactivity* (Oxford University Press, 1987).

[47] S. Heims, "Moment equations for vibrational relaxation coupled with dissociation," J. Chem. Phys. **38**, 603–606 (1963).

[48] A. J. Fangman and D. A. Andrienko, "Vibrational-specific model of simultaneous $N_2 - N$ and $N_2 - N_2$ relaxation under postshock conditions," J. Thermophys. Heat Transfer **36**, 568–583 (2022).

[49] J. D. Bender, P. Valentini, I. Nompelis, Y. Paukku, Z. Varga, D. G. Truhlar, T. Schwartzentruber, and G. V. Candler, "An improved potential energy surface and multi-temperature quasiclassical trajectory calculations of $N_2 + N_2$ dissociation reactions," J. Chem. Phys. **143**, 054304 (2015).

[50] D. A. Andrienko and I. D. Boyd, "Kinetic models of oxygen thermochemistry based on quasi-classical trajectory analysis," J. Thermophys. Heat Transfer **32**, 904–916 (2018).

[51] J. W. Streicher, A. Krish, and R. K. Hanson, "High-temperature vibrational relaxation and decomposition of shock-heated nitric oxide: II. Nitrogen dilution from 1900 to 8200 K," Phys. Fluids **34**, 116123 (2022).

[52] C. Park, "Review of chemical-kinetic problems of future NASA missions. I-Earth entries," J. Thermophys. Heat Transfer **7**, 385–398 (1993).

[53] J. G. Kim and S. M. Jo, "Modification of chemical-kinetic parameters for 11-air species in re-entry flows," Int. J. Heat Mass Transfer **169**, 120950 (2021).

[54] A. Zelechow, D. Rapp, and T. E. Sharp, "Vibrational–vibrational–translational energy transfer between two diatomic molecules," J. Chem. Phys. **49**, 286–299 (1968).

[55] I. V. Adamovich, S. O. Macheret, J. W. Rich, and C. E. Treanor, "Vibrational energy transfer rates using a forced harmonic oscillator model," J. Thermophys. Heat Transfer **12**, 57–65 (1998).

[56] M. L. Da Silva, V. Guerra, and J. Loureiro, "State-resolved dissociation rates for extremely nonequilibrium atmospheric entries," J. Thermophys. Heat Transfer **21**, 40–49 (2007).

[57] S. Ormonde, "Vibrational relaxation theories and measurements," Rev. Mod. Phys. **47**, 193 (1975).

[58] R. L. Taylor and S. Bitterman, "Survey of vibrational relaxation data for processes important in the $CO_2 + N_2$ laser system," Rev. Mod. Phys. **41**, 26 (1969).

[59] E. Garcia, A. Kurnosov, A. Lagana, F. Pirani, M. Bartolomei, and M. Cacciatore, "Efficiency of collisional $N_2 + O_2$ vibrational energy exchange," J. Phys. Chem. B **120**, 1476–1485 (2016).

[60] E. H. Kerner, "Note on the forced and damped oscillator in quantum mechanics," Can. J. Phys. **36**, 371–377 (1958).

[61] G. Oblapenko, "Calculation of vibrational relaxation times using a kinetic theory approach," J. Phys. Chem. A **122**, 9615–9625 (2018).

[62] R. C. Millikan and D. R. White, "Systematics of vibrational relaxation," J. Chem. Phys. **39**, 3209–3213 (1963).

[63] M. L. Da Silva, J. Loureiro, and V. Guerra, "A multiquantum dataset for vibrational excitation and dissociation in high-temperature O_2-O_2 collisions," Chem. Phys. Lett. **531**, 28–33 (2012).

[64] W. Tsang and J. T. Herron, "Chemical kinetic data base for propellant combustion I. Reactions involving NO, NO_2, HNO, HNO_2, HCN and N_2O," J. Phys. Chem. Ref. Data **20**, 609–663 (1991).

[65] Data are collected in https://zenodo.org/records/11220682.

[66] W. Wurster, C. Treanor, and M. Williams, "Non-equilibrium radiation from shock-heated air," Final Report No. AD-A244-905, U.S. Army Research Office, 1991.

[67] C. Treanor and M. Williams, "Kinetics of nitric oxide formation behind 3 to 4 km/s shock waves," Final Report No. AD-A263-653, U.S. Army Research Office, 1993.

[68] S. F. Gimelshein and I. J. Wysong, "Validation of high-temperature air reaction and relaxation models using emission data," J. Thermophys. Heat Transfer **33**, 606–616 (2019).

[69] A. Kosareva, O. Kunova, E. Kustova, and E. Nagnibeda, "Four-temperature kinetic model for CO_2 vibrational relaxation," Phys. Fluids **33**, 016103 (2021).

[70] C. E. Treanor and P. V. Marrone, "Effect of dissociation on the rate of vibrational relaxation," Phys. Fluids **5**, 1022–1026 (1962).

[71] S. P. Sharma, W. M. Huo, and C. Park, "Rate parameters for coupled vibration-dissociation in a generalized SSH approximation," J. Thermophys. Heat Transfer **6**, 9–21 (1992).